

A Coupled PFEM-DEM Model for Fluid-Granular Flows with free surface Dynamics Applied to Landslides

Thomas Leysens, Michel Henry, Jonathan Lambrechts,
Vincent Legat, Jean-François Remacle

June 10, 2025

1 Abstract

Free surface and granular fluid mechanics problems combine the challenges of fluid dynamics with aspects of granular behaviour. This type of problem is particularly relevant in contexts such as the flow of sediments in rivers, the movement of granular soils in reservoirs, or the interactions between a fluid and granular materials in industrial processes such as silos. The numerical simulation of these phenomena is challenging because the solution depends not only on the multiple phases that strongly interact with each other, but also on the need to describe the geometric evolution of the different interfaces. This paper presents an approach to the simulation of fluid-granular phenomena involving strongly deforming free surfaces. The Discrete Element Method (DEM) is combined with the Particle Finite Element Method (PFEM) and the fluid-grain interface is treated by a two-way coupling between the two phases. The fluid-air interface is solved by a free surface model. The geometric and topological variations are therefore naturally provided by the full Lagrangian description of all phases. The approach is validated on benchmark test cases such as two-phase dam failures and then applied to a historical landslide event.

2 Introduction

Fluid mechanics problems involving free surfaces and grains are multifaceted phenomena that require a deep understanding of fluid dynamics and granular interactions. They are particularly relevant to civil engineering, earth science, and many industrial applications.

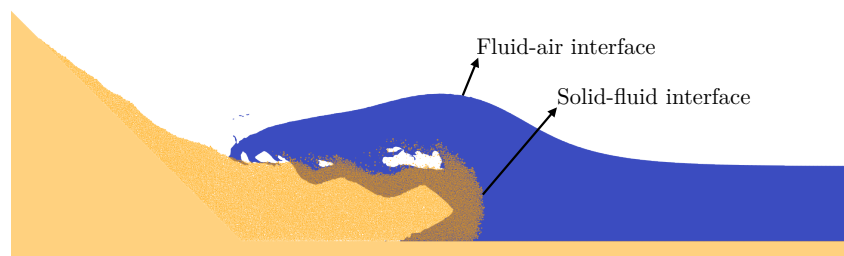


Figure 1: In this study, two types of interfaces are a source of complexity: the free surface between fluid and air, and the solid-fluid interface.

For example, let us consider landslides. These natural phenomena often have catastrophic consequences for people, and understanding the dynamics and predicting the potential impact in advance can help prevent the worst. Landslides occur when soils on steep slopes become unstable. In some cases, these steep hillsides are located above water basins, resulting in a hard impact of the soil on the water, causing significant impulse waves on the water. In other cases, known as submarine landslides, the soil detaches below the water level, creating waves on the water surface. Both cases can be referred to as

landslide tsunamis [41], and it remains a difficult challenge to simulate the creation of these waves near the source, in order to predict their propagation[1]. In these phenomena, the *two main interfaces* are solid-fluid between the moving soil and water, and fluid-air at the surface of the water. Figure 1 is an illustration of the two-dimensional numerical simulation of the Lituya Bay landslide and tsunami, conducted by the authors. This illustrates the complexity of the two types of interfaces.

A numerical solver that performs simulations of this problem must therefore be able to cope with different challenges. On the one hand, interaction laws between the fluid and the granular phase are non-linear. On the other hand, geometrical non-linearities also appear due to the moving interfaces and changes in topology. Our problem thus has two types of interfaces corresponding to specific physical couplings. We will now describe the state of the art in modeling these couplings individually and finally propose a new method that has all the right qualities to simulate all the couplings at once.

2.1 Fluid-air coupling – two phase flows

For the fluid-air coupling, several approaches have been proposed in the literature. Multi-fluid formulations such as volume-of-fluid [20] or level-set [40] approaches simulate both phases completely. However, the cost of doing so can quickly become prohibitive. In fact, the time scales of the dynamics in the lighter, less viscous fluid are often much shorter than in the heavier, more viscous fluid. Much unnecessary work would be spent solving the air phase, which often has limited effect on the flow. In addition, many formulations consider smooth interfaces between the phases because it is difficult to follow topological changes in a sharp manner. This can lead to a loss of accuracy in the representation of the two phases as a result of diffusive effects.

Another strategy consists in simulating only the heavier fluid. This is an attractive solution, as the equations only require to be solved on one part of the domain, and the time step can be chosen at the scale of the dynamics of the heavier fluid. The fluid-air interface thereby becomes a *free surface*, on which the kinematics are dictated by the fact that there is no flow through the interface. The main challenge becomes geometrical. Indeed, the motion of the interface must be tracked and topological changes such as two parts of the domain colliding or separating, should also be accurately detected. It is even possible, as was recently proposed in [25], to account for the presence of a lighter fluid in situations where the heavy fluid fully encapsulates an empty region, such as closing wave phenomena.

Here, Lagrangian approaches are more common, as the degrees of freedom move with the flow. Lagrangian methods can be separated into mesh-based and meshless methods. Meshless methods, typically considered as particle methods, do not require the generation of a mesh, and field gradients are computed using neighborhood samples around the particles. The smoothed particle hydrodynamics (SPH)[30], the material point method (MPM)[38], and the lattice Boltzmann method (LBM)[33] are popular examples of these methods. Mesh-based methods, on the other hand, make use of a mesh connecting the particles to solve the equations of motion. These methods benefit from the strong mathematical background of mesh-based methods, such as the finite element method, to solve the equations and apply boundary conditions. Arbitrary Lagrangian-Eulerian (ALE)[22] belong to this category. They are a good method of choice for simulating deforming domains thanks to great conservation properties, but become complex and prohibitive when high levels of topological changes are desired. Another challenge in these methods remains to efficiently generate meshes onto these particles. With recent advances in mesh generation techniques[28], however, this step should no longer be considered a bottleneck to the entire simulation process.

In this work, the Lagrangian mesh-based method known as the particle finite element method, or PFEM[32], is used. In brief, the PFEM solves the equations of motion using a finite element formulation, and then displaces the nodes of the mesh, the particles, based on the obtained displacement or velocity field. As this Lagrangian displacement may lead to great distortions of the mesh, especially in highly deforming domains such as fluids, the mesh is discarded at each time step, keeping only the nodes, on which a new triangulation is performed. The free surface boundary is then tracked through the use of an indicator function that defines the shape of the domain.

2.2 Fluid-solid coupling

The second interface, between the solid and the fluid, arises as the solid phase is driven into the flow. To model the mixture, *i.e.* the solid grains and the fluid, multiple approaches can be considered. Solid phases can be modeled using solid mechanics and the coupling between the solid and the fluid can be achieved using fluid-structure interaction methods (FSI).

Another approach is to consider the mixture as a continuum described by a two-fluid model. In this case, a constitutive law for the mixture stress tensor must be used [3]. Such a model is well-suited for a macroscopic description of the mixture.

Alternatively, the solid phase can be modeled as a discrete phase composed of individual grains, while the fluid is still a continuum. This approach is commonly referred to as CFD-DEM, which couples Computational Fluid Dynamics with the Discrete Element Method. The discrete representation of the solid allows to describe local interactions between grains, such as collisions. To model these contacts, two methods are commonly used: the smooth contact dynamics and the non-smooth contact dynamics, also called the hard sphere model. In the smooth contact dynamics, the contact forces are computed using an explicit penalty method based on the overlap of the grains [24]. In the non-smooth contact dynamics, contact impulses are iteratively obtained by prohibiting grain overlaps [23]. Both approaches are able to efficiently and accurately describe contact forces, taking into account frictional and cohesive behaviours if needed.

To capture the grain presence in the fluid without the need to track the exact interface, volume-averaged methods can be used. The fluid equations are averaged on cells larger than the particle size [2]. The forces between the two phases are computed using the averaged stress tensor and additional constitutive laws. Still, satisfying Newton's third law is mandatory to ensure the conservation of momentum. To this end, a strategy to project the forces caused by the grains as well as their volume onto the fluid mesh are required. An extensive review of the different methods to compute the void fraction is presented in [7]. The most common approach, the particle centroid method (PCM), assumes grains to be described by their centroid on which forces can be estimated. A smooth representation of the void fraction can then be obtained through a two-stage projection as proposed by [26]: first, a nodal non-negative void fraction is computed. Next, a diffusion operator smooths the field. Alternatively, the solid volume ratio can be estimated at quadrature points leading to a temporally stable scheme [13]. This approach allows the mesh to be around the same size as the grains, which is a significant improvement compared to the PCM which is typically restricted to a mesh size larger than the grain diameter.

In this work, the mesh size limitation is overcome by computing the exact centroid between the mesh elements and each grains. This method uses a first degree integration rule over the grain and an exact void fraction computation [36]. This is suitable for the simulations performed in this work, as the mesh size will be refined close to the free surface independently of the grain size.

2.3 Fluid-Granular Flows with free surface Dynamics

The present work aims at simulating granular free surface flows. The applications require to have sharp interfaces between the fluid, the air and the solid, and allow large deformations of the domain. Different approaches for simulating free surface flows coupled to a solid granular formulation have been proposed. Eulerian-Lagrangian methods such as FEM-DEM couplings with a multi-phase flow formulation have been proposed, for instance [27]. In their approach, the free surface interface is captured using a conservative levelset method, while the solid-fluid interface is managed by an immersed boundary method. Such approaches benefit from high levels of accuracy and good conservation properties. The fact of requiring a levelset function to represent the fluid domain, however, may increase the computational cost and strong topological changes are often complicated to capture.

Lagrangian-Lagrangian formulations have also been proposed, such as a moving particle semi-implicit (MPS) formulation for the fluid, coupled with the DEM method for the solid granular phase [42]. Similarly, an SPH-DEM coupled formulation was proposed by [39]. In both methods, local gradients are defined through the use of a smoothing kernel based on neighboring particles, and therefore do not require the proper definition of a mesh. An important aspect of the coupling between the fluid and solid

phases in this method is that a large number of fluid particles is required around each solid particle, and this ratio should be kept constant. Simulating solid impacts on the free surface (*i.e.*, solid particles entering the fluid) may therefore be challenging.

In [15], a fully Lagrangian approach was proposed to simulate landslide phenomena, in which both phases are considered as a continuum. More specifically, both phases are simulated with the particle finite element method, but two different constitutive models are considered for each phase. While the water phase is modeled as a standard Newtonian fluid, the landslide phase is parametrized using a frictional viscoplastic model. Three-dimensional results were demonstrated and used to simulate the 1963 Vajont rockslide and tsunami.

Finally, a PFEM-DEM formulation has been proposed by Franci et al. [16] for a one-way coupling for particle-laden flows. Since the particles are sufficiently small and disperse such as to consider their effect on the fluid as negligible. Hence, the approach of Franci et al. is very similar to the method proposed in this paper, albeit without the two-way coupling.



Figure 2: We present a fully coupled PFEM-DEM formulation for the simulation of fluid-grain flows with strong domain deformations.

In this paper, we present a new PFEM-DEM formulation to simulate two-way coupled fluid-grain problems with large deformations of the fluid domain. Figure 2 demonstrates the potential of our solver. Deforming free surfaces, fluid-grain coupling, complex evolutions of the domain and moving boundaries are all within the capabilities. This method is of great interest for simulations such as landslide-generated impulse waves. Although the rotating turbine is an illustrative example, the present paper aims to validate our approach to landslide-related problems. Indeed, thanks to the Lagrangian formulation of the fluid, free surfaces are inherently captured, allowing to simulate strongly dynamic phenomena such as impulse waves. The discrete element method, used for the granular phase, is adequate for the landslide phenomena simulated in this paper, but also has the capability to simulate phenomena at much smaller scales, understating the versatility of the approach.

We first present the fully coupled formulation, followed by two benchmarks to validate the approach.

Finally, we apply the method to the 1958 Lituya Bay landslide and tsunami, a historical event.

3 The Physical Problem

In this section, the governing equations of the physical problem are presented. The fluid flow within the multi-phase system is governed by the Volume-Averaged Navier-Stokes (VANS) equations. The motion of individual grains is modelled using the Newton-Euler equations, assuming the grains to be rigid bodies with a cylindrical shape. Interactions between grains, as well as between grains and the boundaries, are handled by the Non-Smooth Contact Dynamics (NSCD) method [23]. To represent the grains in the weak form of the VANS equations, a least-squares projection of the relevant grain fields is used.

In the following, the fluid governing equations are presented in Section 3.1, followed by the equations for the grains in Section 3.2, and finally the fluid-grains coupling model is discussed in Section 3.3.

3.1 Volume-Averaged Navier-Stokes equations

These fluid conservation equations are derived by averaging the Navier-Stokes equations over a control volume containing both phases, similar to a two-fluid approach. The Lagrangian formulation is used to track the fluid material points. This description provides a natural way to capture the domain deformation and the free surface dynamics.

$$\frac{d\mathbf{x}}{dt} = \mathbf{u}, \quad (1)$$

$$\nabla \cdot (\varepsilon \mathbf{u} + (1 - \varepsilon) \mathbf{v}) = 0, \quad (2)$$

$$\varepsilon \rho \frac{d\mathbf{u}}{dt} = \nabla \cdot \boldsymbol{\sigma} + \varepsilon \rho \mathbf{g} + (1 - \varepsilon) \mathbf{f}, \quad (3)$$

where \mathbf{x} is the fluid material point position, \mathbf{u} is the fluid velocity, \mathbf{v} is the averaged solid velocity, ρ is the fluid density, $\frac{d}{dt}$ the material derivative in the Lagrangian frame, $\boldsymbol{\sigma}$ is the Cauchy stress tensor, \mathbf{g} is the gravitational acceleration, ε is the void fraction and \mathbf{f} is the fluid-grain interaction force. The stress tensor is defined as

$$\boldsymbol{\sigma} = -p\mathbf{I} + \varepsilon\eta(\nabla\mathbf{u} + \nabla^T\mathbf{u}), \quad (4)$$

where p is the pressure, \mathbf{I} is the identity tensor, and η is the dynamic viscosity. The displacement, Equation (1), is performed at the nodal values, Section 4.7 describes the proposed scheme. The continuity equation and momentum conservation equation, Equations (2) and (3), are solved using the Finite Element Method. Linear elements are used for both the velocity and pressure fields. Let τ_i denote the shape functions associated to the i -th node, the discretisation of the velocity and pressure are given by

$$\mathbf{u}(\mathbf{x}, t) \approx \mathbf{u}^h(\mathbf{x}, t) = \sum_{i=1}^N \mathbf{u}_i(t) \tau_i(\mathbf{x}(t)), \quad (5)$$

$$p(\mathbf{x}, t) \approx p^h(\mathbf{x}, t) = \sum_{i=1}^N p_i(t) \tau_i(\mathbf{x}(t)), \quad (6)$$

where \mathbf{u}^h and p^h are the discrete velocity and pressure fields, respectively, N is the number of nodes in the mesh, and \mathbf{u}_i and p_i are the nodal values of the velocity and pressure fields. As equal-order discretisation does not satisfy the inf-sup condition, a Pressure-Stabilizing Petrov-Galerkin (PSPG) is introduced [21]. The discrete form of the volume-averaged equations is to find $(\mathbf{u}^h, p^h) \in (\mathcal{U}^h \times \mathcal{P}^h)$ such that for all test functions $(\hat{\mathbf{u}}, \hat{p}) \in (\hat{\mathcal{U}}^h \times \hat{\mathcal{P}}^h)$,

$$\begin{aligned}
0 &= \int_V \nabla \cdot (\varepsilon \mathbf{u}^h + (1 - \varepsilon) \mathbf{v}^h) \hat{p}^h \, dV \\
&+ \sum_i^N \xi \int_V \mathbf{R}(\mathbf{u}^h, p^h) \cdot \nabla \hat{p}^h \, dV,
\end{aligned} \tag{7}$$

$$\begin{aligned}
0 &= \int_V \left(\overbrace{\varepsilon \rho \frac{d\mathbf{u}^h}{dt} + \nabla p^h - \varepsilon \rho \mathbf{g} - (1 - \varepsilon) \mathbf{f}^h}^{\mathbf{R}(\mathbf{u}^h, p^h)} \right) \cdot \hat{\mathbf{u}}^h \, dV \\
&- \int_V \nabla \cdot \left(\varepsilon \eta \left(\nabla \mathbf{u}^h + \nabla^T \mathbf{u}^h \right) \right) \cdot \hat{\mathbf{u}}^h \, dV,
\end{aligned} \tag{8}$$

where $\mathbf{R}(\mathbf{u}^h, p^h)$ is the residual of the momentum equation and ξ is the PSPG stabilization parameter obtained element-wise as

$$\xi = \left[\left(\frac{2}{\Delta t} \right)^2 + \left(\frac{4\eta}{\rho h^2} \right)^2 \right]^{-\frac{1}{2}}. \tag{9}$$

No advection is considered in the discretisation of the momentum equation, as the advection is captured by the nodal displacement, see Section 4.7. The viscous term is not considered in the momentum residual as its derivative is zero for linear shape functions. Details can be found in [8, 19] regarding the integration by parts of the equations and the application of boundary conditions. The fluid-grain model is presented in Section 3.3 and its implementation is described in Section 4.

3.2 Grains dynamics

Grains are assumed to be circular rigid bodies with a prescribed radius and mass. Their dynamics are governed by the Newton-Euler equations:

$$\frac{d\mathbf{y}}{dt} = \mathbf{v}, \tag{10}$$

$$m \frac{d\mathbf{v}}{dt} = m\mathbf{g} + \mathbf{F}_c + \mathbf{F}, \tag{11}$$

$$I \frac{d\boldsymbol{\omega}}{dt} = \mathbf{M} + \mathbf{M}_c, \tag{12}$$

$$\mathcal{C}(\mathbf{F}_c, \mathbf{M}_c, \mathbf{v}, \mathbf{y}) = 0, \tag{13}$$

where m are the grain masses, \mathbf{y} are the grain positions, \mathbf{v} are the grain velocities, I are the moments of inertia, $\boldsymbol{\omega}$ are the grain angular velocities, \mathbf{F} are the fluid-grain forces, \mathbf{F}_c are the contact forces, \mathbf{M} are the fluid-grain torques and \mathbf{M}_c are the contact torques. Contacts between grains and the boundaries are modelled using the Non-Smooth Contact Dynamics (NSCD) assuming inelastic collisions. The abstract contact dynamics operator \mathcal{C} is used to enforce the contact conditions, Equation (13). For each contact, these conditions are the Signorini condition, Coulomb's friction law and the momentum balance at the contact point. The Signorini condition ensures that the grains do not overlap at the end of the collision. Coulomb's friction law ensures that, at the contact point, the relative velocity of the grains remains within the tangential cone. The contact dynamics describes the relative velocity of two grains after the collision to the contact impulse. A detailed description of this methodology can be found in [11, 10, 8]. The fluid-grain interaction force relies on constitutive laws for local interactions not captured by the numerical scheme. In this work, solely the drag force and pressure gradient are considered, the lift force, Basset history force and virtual mass force are neglected. Hence, the fluid-grain force associated to the grain index p is

$$\mathbf{F} = \int_{V_p} \left(\mathbf{f}_p^{\text{drag}} - \nabla p \right) dV_p, \quad (14)$$

where V_p is the volume of the grain, and $\mathbf{f}_p^{\text{drag}}$ is the drag force acting on the grain. The drag force density is modelled using the Dallavalle correlation with the Di Felice voidage function,

$$\mathbf{f}_p^{\text{drag}} = \underbrace{\varepsilon^{-2.8} \left(0.77 \sqrt{\varepsilon \text{Re}_p} + 5.88 \right)^2}_{\triangleq \gamma} \frac{\eta}{d_p^2} \left(\mathbf{u} - \mathbf{v}_p \right), \quad (15)$$

where d_p is the grain diameter, $\text{Re}_p = \rho d_p \|\mathbf{u} - \mathbf{v}_p\| / \eta$ is the Reynolds number and γ is the drag coefficient. No angular velocity is considered in the fluid-grain force calculation.

3.3 Fluid-grains coupling

As grains are discrete entities flowing within the fluid domain, a coupling strategy is required to include them in the VANS equations. This is achieved through an L_2 -projection step, in which grain fields are projected over the domain. Three fields are of interest, the void fraction to ensure mass conservation, the grain velocity to ensure fluxes are correctly computed, and the fluid-grain interaction force to ensure momentum conservation and Newton's third law are satisfied. The projections are defined as,

$$\int_V (1 - \varepsilon) \tau dV = \sum_p \int_{V_p} \tau dV_p, \quad (16)$$

$$\int_V (1 - \varepsilon) \mathbf{v}^h \cdot \nabla \tau dV = \sum_p \int_{V_p} \mathbf{v}_p \cdot \nabla \tau dV_p, \quad (17)$$

$$\int_V (1 - \varepsilon) \mathbf{f}^h \tau dV = - \sum_p \int_{V_p} \left(\mathbf{f}_p^{\text{drag}} - \nabla p^h \right) \tau dV_p, \quad (18)$$

where, as a reminder, τ represents the nodal shape functions. In order to avoid overshoots and undershoots due to the L_2 projection, the mass matrix is mass-lumped for the void fraction, Equation (16). The left-hand side of Equations (17)–(18) is substituted by the right-hand side in the discrete form of the VANS equations (7)–(8). An ad-hoc integration scheme is performed to integrate over the grain domain by subdividing the grain into the mesh intersected elements. Over each element that intersects the grain, the centroid of the overlapping area is computed and used to evaluate the fields. Figure 3 illustrates the projection of grain volume to the fluid domain to compute the void fraction, and the centroid of the grain-triangle element overlap are indicated in red. Details on the spatial representation of the grains are discussed in section 4.5.

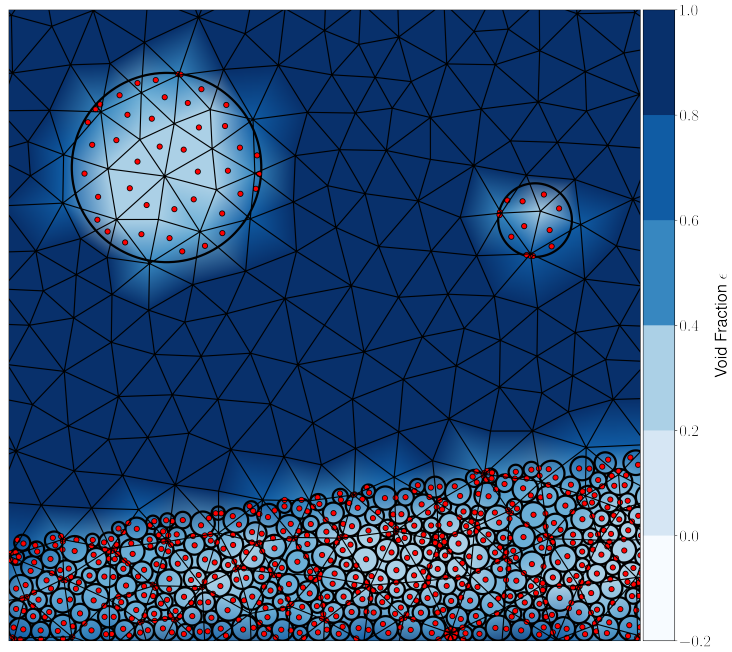


Figure 3: Illustration of the fluid-grains coupling. Grains are represented as a continuous field using an L_2 projection. The integral over the disc is approximated by the sum of the integrals over the elements containing the grain. The red dot represents the centroid of each overlapped sub-element. The void fraction is indicated by the colour map.

4 A fully Lagrangian scheme

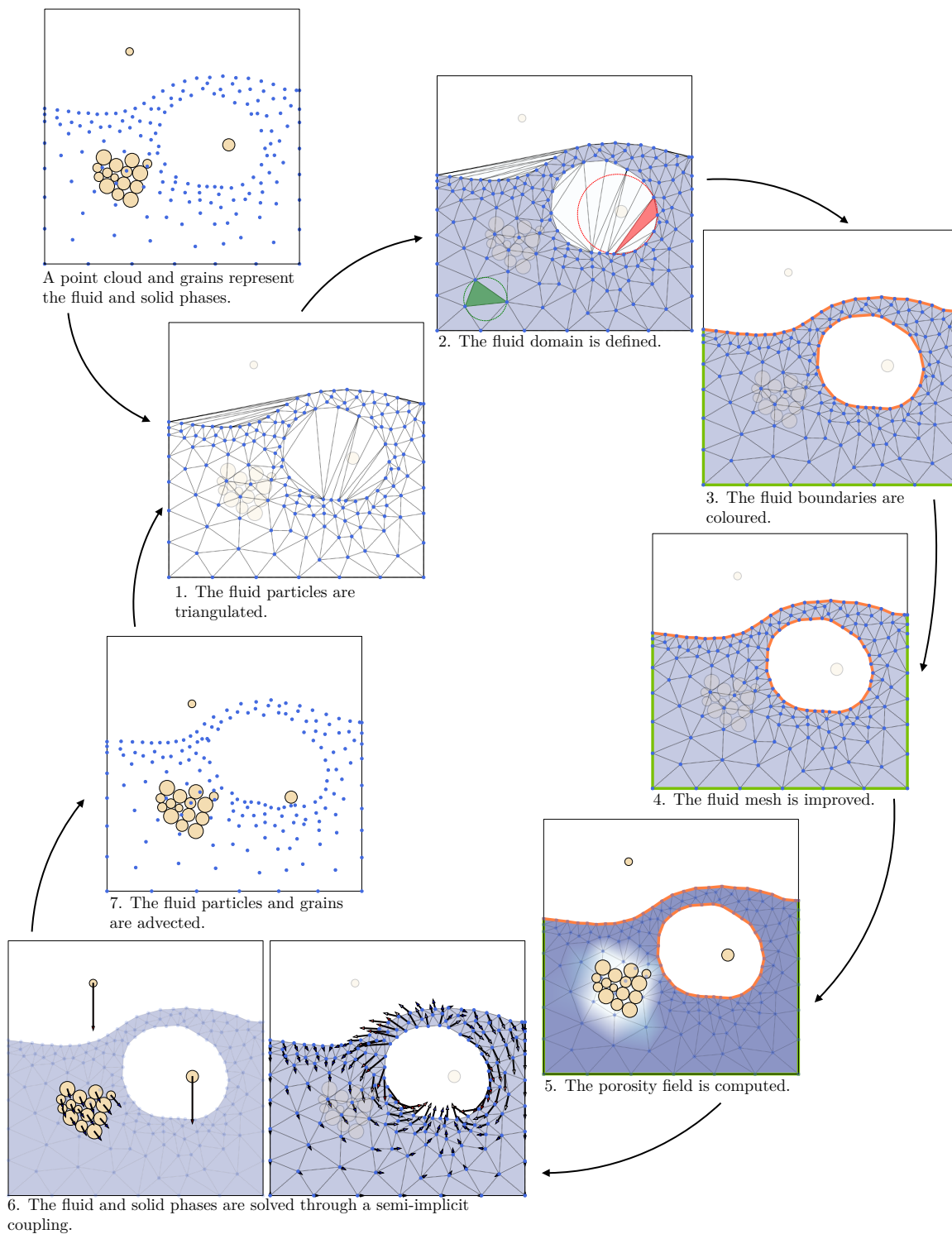


Figure 4: A schematic of the algorithm.

The simulations of interest in the current study occur in extremely strongly deforming domains. This is the case for both the solid phase and the fluid phase. For this reason, considering Lagrangian formulations, inherently capable of describing the motion and deformations of the domains, is crucial. The decision was therefore made to adopt a particle-based formulation for both phases.

This not only allows to track topological changes in both phases, but also to naturally couple them together. Hence, both phases are initially represented by two separate sets of particles: the grains and the fluid. This is the starting point of the overall algorithm of the coupled method, presented in Figure 4. This figure will help the reader understand the algorithm. In what follows, the fluid discretization approach is presented first, followed by the solid-fluid coupling procedure to integrate the equations in time and space. Finally, the advection steps for both the fluid particles and solid grains are described.

4.1 Fluid particles triangulation

Capturing highly deforming fluid domains requires a specific technique that inherently follows the evolution of the geometry. The particle finite element method has been specifically designed for such flows. In this Lagrangian method, all the relevant information is passed on from one time step to another through the particles. Then, with the aim to solve the equations of motion, a Delaunay triangulation of these particles is performed, resulting in a mesh of the convex hull (Figure 4: point 1).

4.2 Domain definition

The particles are displaced after each time step in such a way that it is impossible to simply deform the initial mesh. In addition to the *tracking* of the interfaces in a continuous manner, the topological changes appearing near free surfaces must also be taken into account. We thus only rely on a point cloud S to represent the fluid domain and its boundary. It is possible (and fast) to triangulate S and the boundary of this triangulation will give the new ‘shape’ of the fluid domain. The *convex hull* $H(S)$ of a point cloud $S = \{s_1, \dots, s_n\}$ is a clear and perfectly defined concept. However using $H(S)$ as the *oracle* that determines the boundary of the fluid domain is not very interesting. Being always convex, it is obviously very restrictive. Figure 5 illustrates the importance of having a method that accurately covers something else than a convex hull.

The very notion of the boundary of a point cloud is not unique. There are a large number of methods that can be used to calculate the boundary of S , one being called the α -shape of S [12]. The concept of α -shape is closely linked to the Delaunay triangulation $DT(S)$. The α -complex of S is the set of triangles of $DT(S)$ whose circumradii are smaller than a given length. The α -shape of S is the boundary of the α -complex.

To capture the evolution of the shape of the fluid domain, we compute $DT(S)$ and subsequently remove triangles that are too large (see Figure 4: point 2). We verify that the circumradius R_e of each element satisfies the following criterion:

$$R_e < \alpha \cdot h(\mathbf{x}). \quad (19)$$

Here, $h(\mathbf{x})$ is a mesh size field that defines how acceptable circumradii are distributed over the domain. In this context, the parameter $\alpha \geq 1$ corresponds to a tolerance. Size fields are continuous functions of the position \mathbf{x} and meshes are discrete, so we allow some long edges/large elements to be acceptable.

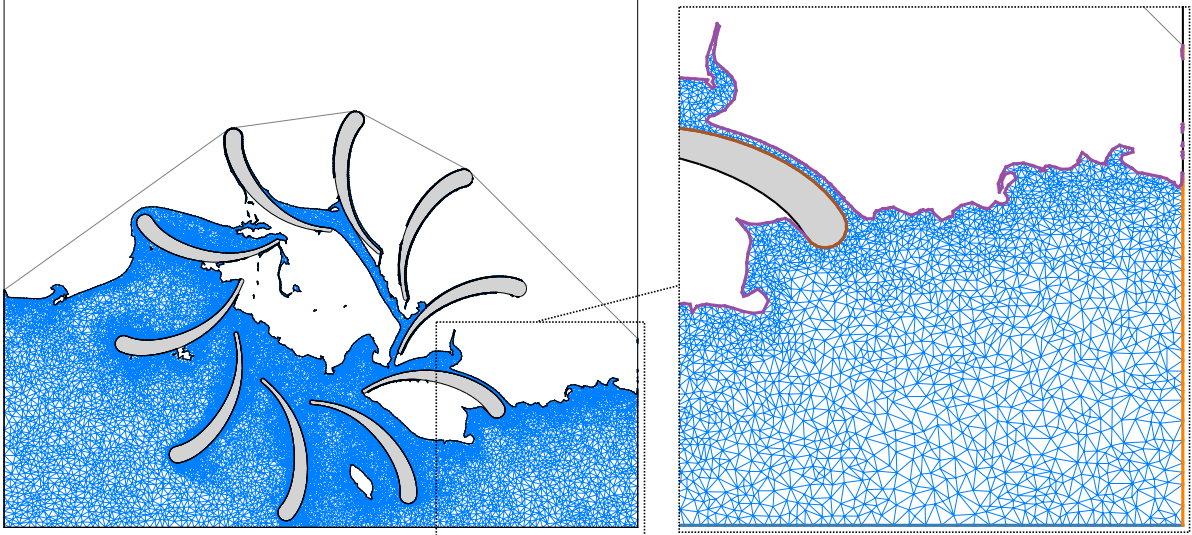


Figure 5: Chaotic free surface flows require the method to be able to track complex topological changes and to detect boundaries.

4.3 Boundary colouring

In Lagrangian formulations, it is not possible to define the boundaries only once at the beginning of the simulation. Indeed, since the particles follow the deformation of the fluid and its topological changes, interactions with the walls surrounding the fluid will also change over time. Boundaries therefore need to be identified again at the beginning of each time step, so that the correct boundary conditions can be applied. This is even more critical in cases of moving boundaries, as illustrated in Figure 5. From the α -shape algorithm, the boundaries of the fluid domain are automatically obtained. However, the distinction between different boundaries such as walls, moving bodies and free surfaces is not automatic, and therefore, the fluid boundary edges must be coloured according to which boundary wall they belong. In Figure 4, point 3, fluid boundaries belonging to the wall are coloured in green, and free surfaces in red.

Classical PFEM implementations consider a discretisation of the wall boundaries, in which the nodes of the walls are actually part of the fluid if an element can be created with them that is accepted by the α -shape. In the method proposed here, walls are not explicitly meshed, and the fluid only recognises them geometrically. Figure 6 illustrates the difference between these two approaches. The main advantage of the classical method, which considers particles along the wall, is that it is very simple to implement and boundaries of the fluid can be immediately identified as part of a specific wall. The main disadvantage is that this is known to cause issues in terms of mass conservation, as has discussed in [14]. Moreover, properly applying slip boundary conditions can be complex.

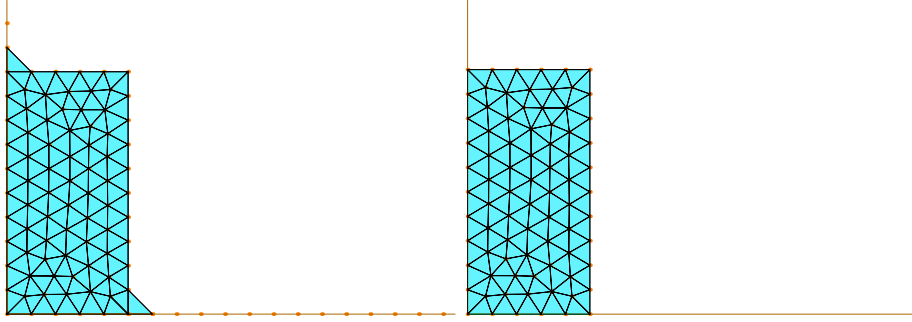


Figure 6: Comparison between the classical PFEM method for wall boundary management in which boundary nodes are considered along solid walls (l), and our approach which only considers solid walls if fluid particles are actually on it (r).

Figure 7 illustrates the steps followed by the boundary management proposed in this work. First of all, we define a one-dimensional boundary mesh to represent the solid walls. This mesh is constituted of a sequence of edges. Once the boundary walls are defined, every edge of the wall is stored into a quadtree data structure [29]. This allows to perform efficient queries to detect if fluid particles are approaching walls.

The quadtree data structure is then used to colour de boundaries. Once the α -shape algorithm has defined the boundaries of the fluid, a loop is performed over all the bounding edges of the α -shape. If the two fluid particles of a bounding edge are situated on a wall edge of the quadtree, the edge is colored such that it belongs to the wall. In practice, being *on a wall edge* means that the two particles are within a small distance to the wall, for instance a distance less than 1% of the mesh size.

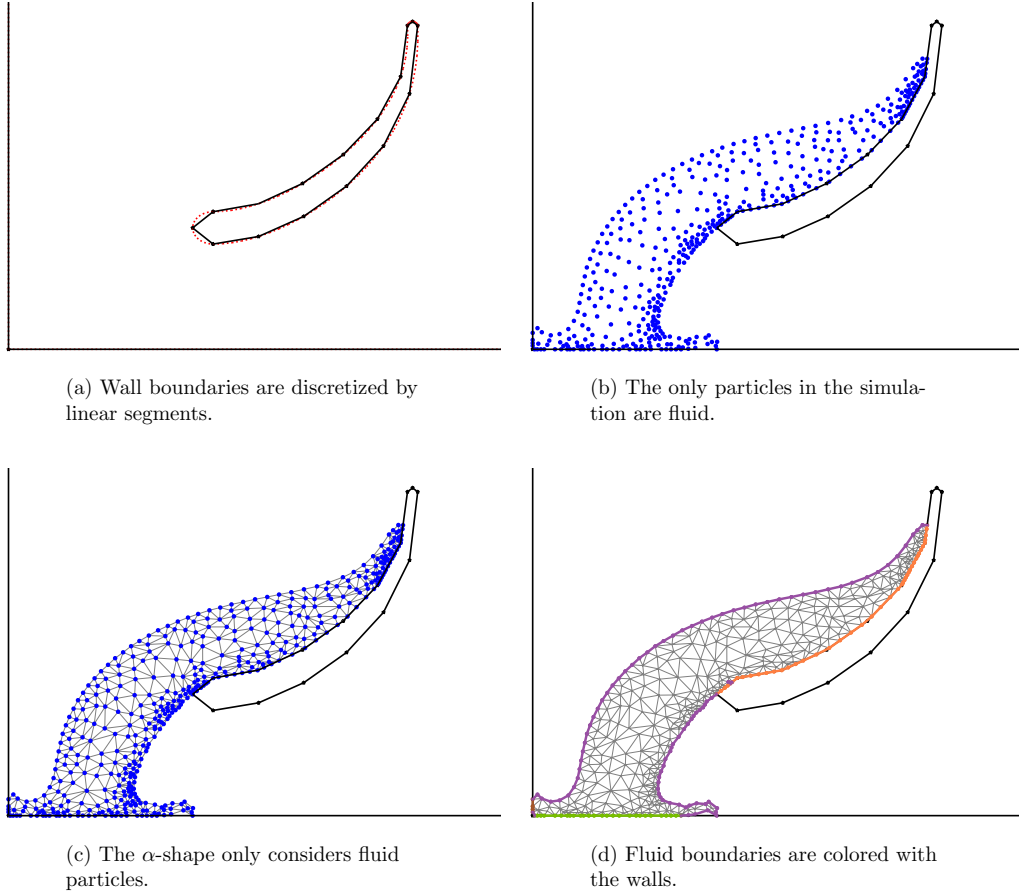


Figure 7: The different steps of the wall detection method.

Applying boundary conditions then becomes straightforward, and can be done in the same manner as any classical finite elements formulation. The issue of fluid particles crossing solid boundaries is addressed in the advection step, described in section 4.7.

4.4 Mesh adaptation

Mesh adaptation is crucial in the PFEM. Indeed, since the definition of the fluid domain relies on the α -shape, one must ensure that the elements inside the fluid domain respect the given size field and respect condition (19). Due to the Lagrangian motion of the particles, the triangulation will be deformed. This can lead to very poor quality elements in the mesh, and consequently a poor definition of the fluid domain and its boundaries.

In [25], an adaptive mesh refinement technique has been proposed for the PFEM to address this challenge. The size field $h(\mathbf{x})$, used to filter elements in the α -shape procedure, is chosen to be highly refined near the free surface, and coarser at a distance from these boundaries. Indeed, since it is near the free surface that the topological changes occur, it is desirable to have greater accuracy in these regions. After defining the boundaries of the fluid domain through the α -shape, an algorithm broadly inspired by the constrained Delaunay technique of Chew [6] is then used to meet the quality and size criterion imposed by the size field. This method allows to maintain high quality elements at all times, and ensures a smooth and continuous representation of the free surface. An interpolation of the solution is performed on newly inserted nodes.

4.5 Spatial representation of grains in the fluid

Since grains are represented as discrete entities, they are projected onto the continuous representation of the fluid, Equations (16)–(18).

To compute the void fraction and the averaged velocity of the grains, the mass-matrix, which arises on the left hand-side of the weak form, is mass-lumped [5, 18]. Conversely, the fluid-grain interaction force is computed locally for each grain and then applied to the fluid. This is done to ensure Newton’s third law.

To represent a grain, the disc is subdivided by mesh facets, generating sub-elements. The centre of mass of each sub-element is computed analytically by iterating over the edges of the overlapped element. For each edge, a triangle is constructed using the edge and the grain’s centre of mass. The exact intersection between this triangle and the disc is computed, along with the centroid of the intersection as it is only composed of triangles or disc sections. Using these centroids, the centre of mass of each sub-element is determined, on which the integrand is then evaluated. Figure 8 illustrates this procedure.

This approach allows for the exact integration of a linear integrand over the intersection, ensuring that the void fraction is computed precisely while maintaining positive values bounded by unity. Additionally, if a grain spans multiple elements, the interaction force is distributed across the elements containing the grain, rather than being concentrated at the grain’s centre of mass. This distribution smooths out jumps in the fluid-grain interaction force when a grain enters or leaves an element.

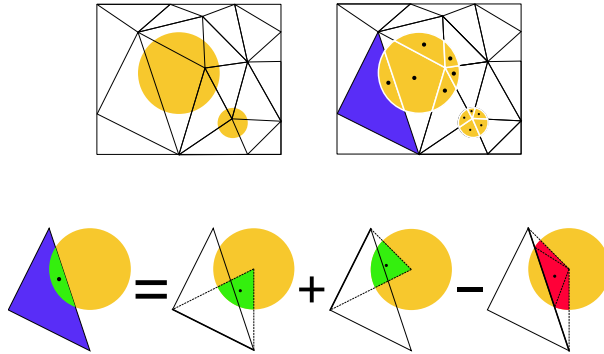


Figure 8: Disc integration rule over the fluid domain. The disc is divided into sub-elements defined by the overlap with each element of the mesh. The centroid of each sub-element is computed by iterating over the element edges. The black dot indicates the computed centroid.

4.6 A semi-implicit temporal scheme

Since the fluid-grain interaction force is a source term in the momentum equation, it is crucial to ensure the stability of the numerical scheme as its magnitude can be significant. This is achieved by using a semi-implicit scheme to estimate the fluid-grain interaction force. The grain index p is dropped for clarity. The force is linearised and an implicit prediction of the grain velocity at the integration point is made based on the grains dynamics, Equation (11),

$$m \frac{\mathbf{v}^* - \mathbf{v}^n}{\Delta t} = m\mathbf{g} + \mathbf{F}_c^n + V \left[-\nabla p^{n+1} + \gamma^n (\mathbf{u}^{n+1} - \mathbf{v}^*) \right] \quad (20)$$

where subscript ‘ n ’ denotes the explicit value, subscript ‘ $n + 1$ ’ the implicit value, and subscript ‘*’ the predicted value. As the contacts have not been resolved yet, the contact force is taken as the one estimated at the previous time step. It leads to the following prediction of the grain velocity at the integration point,

$$\mathbf{v}^* = \left[\frac{m}{\Delta t} + \gamma^n \right]^{-1} \left[\frac{m}{\Delta t} \mathbf{v}^n + m\mathbf{g} + \mathbf{F}_c^n + V \left(-\nabla p^{n+1} + \gamma^n \mathbf{u}^{n+1} \right) \right] \quad (21)$$

This estimate is then used to compute the drag force acting on the fluid, Equation (15), and to project the grain mass flux in the continuity equation, Equation (2). An implicit Euler scheme is applied to the viscous term in the momentum equation, Equation (3).

As the mesh can reach fine resolutions to capture topology changes, the void fraction can tend to zero if an element is completely covered by a grain. In this case, the drag force tends to infinity, leading to a non-physical force. Additionally, the fluid acceleration, stress tensor and gravitational force terms vanish in the momentum equation. The only term remaining is the drag force, which imposes the velocity continuity in the grains domain. The pressure field is computed based on the velocity prediction in the continuity equation. As the prediction is based on the pressure gradient and the fluid velocity, the system of equations stays full-rank even though the void fraction tends to zero. In practice, to avoid large non-physical forces, a minimal value of 10^{-8} is set for the void fraction.

4.7 Advection

The final step in the algorithm consists in displacing the fluid particles and solid grains using their obtained Lagrangian velocities. For the fluid, the positions are updated using a second-order scheme that approximates the acceleration of the particles using the difference in velocities between the previous and current time step. We consider the scheme proposed in [37]. This choice for a second-order scheme is important in order to ensure better conservation properties near the interfaces. The grains are updated using a first-order implicit Euler method, which results from the iterative contacts solver.

$$\mathbf{x}^{n+1} = \mathbf{x}^n + \mathbf{u}^{n+1} \Delta t + \frac{\mathbf{u}^{n+1} - \mathbf{u}^n}{\Delta t} \Delta t^2 \quad (22)$$

$$\mathbf{y}^{n+1} = \mathbf{y}^n + \mathbf{v}^{n+1} \Delta t, \quad (23)$$

For the fluid phase, a final step is required here to account for solid boundaries. Indeed, since the fluid boundaries are defined at the beginning of each time step, it is essential to ensure that boundary conditions are accurately applied despite the explicit nature of the position update. In many PFEM approaches [4, 31] for fluid simulations, solid boundary particles are fixed on the walls, and define solid walls to which boundary conditions are then applied. The approach followed here, however, allows for a straightforward application of slip-boundary conditions along solid walls by considering only fluid particles and representing the walls only geometrically. For particles which are, at the beginning of the time step, already on a wall, slip boundary conditions can be applied without any difficulty through the finite element formulations. For fluid particles that cross a solid wall during a time step due to the explicit update, Equation (22), a correction is made on these particles' velocities to project them on the boundary, as illustrated in Figure 9.

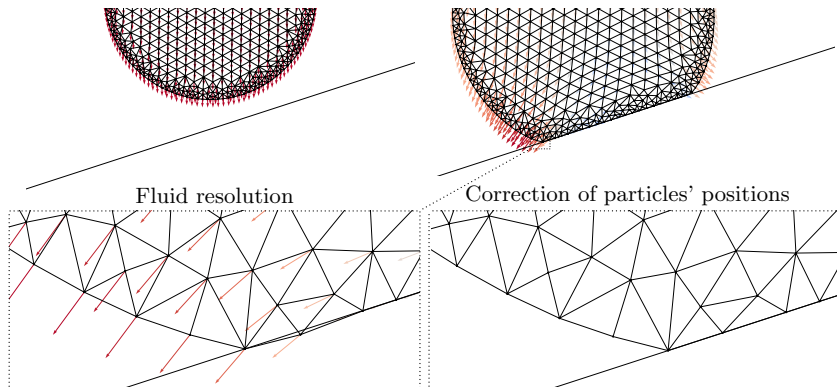


Figure 9: The position of the particles that cross a wall during the advection step is corrected by projecting them on the wall.

Both the fluid and the solid phases are treated with an implicit scheme for to integrate the velocity in time, therefore no stability conditions arise. In order to ensure an accurate advection of the fluid material points, the fluid time step is chosen as $\Delta t_f = \mathcal{O}\left(\frac{h_{\min}}{\|u_{\max}\|}\right)$. The solid time step is governed by the contact solver which is based on the Non-Smooth Contact Dynamics method. It consists in finding iteratively the contact impulse such that no overlap occurs at the end of the time step, without the need for stiffness-based penalty parameters. At each time step, first a contact detection is performed, then the contact impulse is computed and finally the solid phase is updated. In order to limit the number of potential contacts in the detection step, the solid time step is chosen as $\Delta t_s = \mathcal{O}\left(\frac{d_{\min}}{\|v_{\max}\|}\right)$. The potential mismatch between fluid and solid time steps is handled by a sub-stepping strategy for the solid phase. In practice, sub-stepping is only required during the initial stages of the simulation, when mesh elements remain large and the fluid motion is slow. The maximum sub-stepping observed in the simulations presented in this work is five.

5 Validations

In this section, two experiments serve to verify and validate the proposed method. The first is a collapse of a partially filled water column, commonly referred to as a dam break. The second is a collapse of a column of grains into a water bed. The results are compared with references from the literature. In all of the experiments presented, the flow is driven by gravitational effects. Hence, the Froude number is chosen as a dimensionless number to characterize the experiment as it measures the ratio of inertial forces to gravitational forces,

$$\text{Fr} = \frac{v}{\sqrt{gh}}$$

where v is a characteristic velocity, computed as an equivalent velocity if the water or granular column were to accelerate in free fall over a distance corresponding to half of its height h . The characteristic length and velocity that define the Froude number can then also be used to define non-dimensional times and lengths.

All the simulations presented next are simulated with free-slip boundaries along solid walls

$$\begin{cases} \mathbf{u} \cdot \mathbf{n} = 0, \\ \mathbf{t} - (\mathbf{t} \cdot \mathbf{n})\mathbf{n} = \mathbf{0}, \end{cases}$$

where \mathbf{n} is the outward facing normal and $\mathbf{t} = \boldsymbol{\sigma} \cdot \mathbf{n}$ is the Cauchy stress vector. In other words, a zero-velocity condition is imposed in the normal direction, and no stresses are applied in the tangential direction. A free surface is considered at the interface between water and air:

$$\mathbf{t} = p_0\mathbf{n} - \kappa\gamma\mathbf{n},$$

where p_0 is an external atmospheric pressure, κ is the curvature at the free surface, and γ is the surface tension coefficient.

5.1 Dam break

In this first verification test case, a water column is initially at rest between three walls. A set of grains are immersed into the water column. The total mass of the grains is 200g, and their radius is 1.35mm, resulting in a total of 279 grains. A Coulomb friction law is used to model tangential interactions between grains with a friction coefficient of 0.2. No friction is considered between the grains and the walls. Surface tension is considered at the water-air interface, with a coefficient of 0.0072N/m. The wall left to the water column is a vertically sliding gate, which is lifted at $t = 0$ with a velocity of 0.68 m/s. The water column and immersed grains are then free to slide under the gate, into the empty portion of the container. The initial setup with dimensions of the water column is presented in Figure 10. Along the walls, a free-slip boundary condition is imposed.

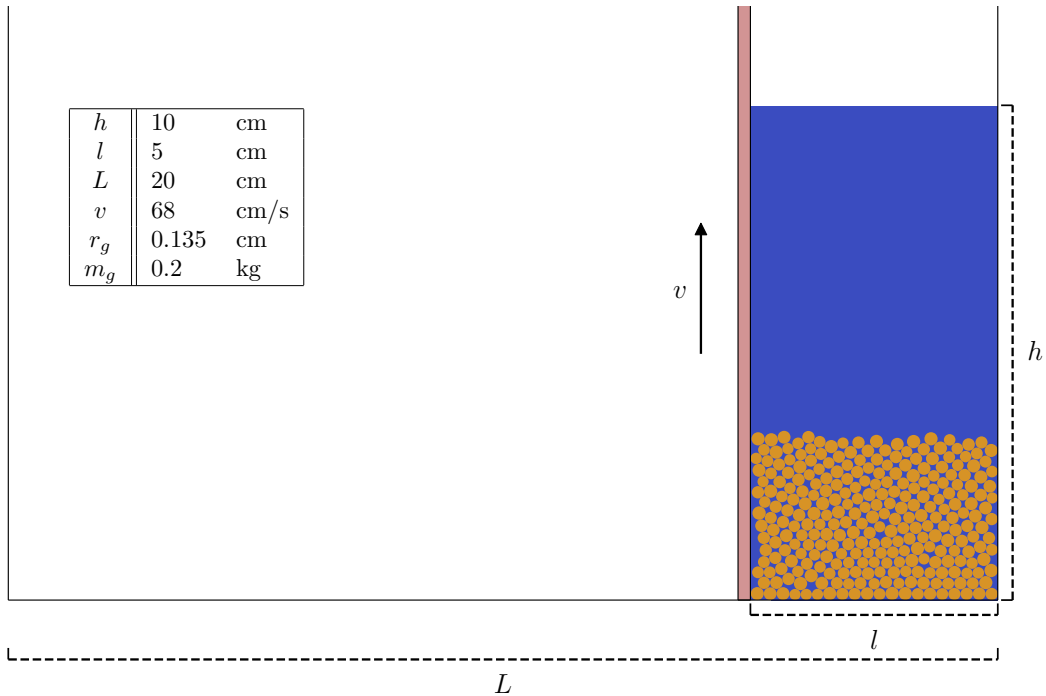


Figure 10: Dam break test case setup.

The experiment can be divided into three main steps. First, the water and grain mixture slides into the open space. Two fronts, the fluid and the grain front, travel along the bottom in a clearly distinguishable wave. The timing of this first phase is from around 0 to 0.2s. Then, the wave hits the left wall, causing the mixture to rise and eventually collapse onto itself. This generates high levels of turbulence, leading to chaotic phenomena such as splashing and trapped air bubbles. The final step is a chaotic sloshing motion in the container, which eventually reduces to reach a final, steady state. Figure 11 shows snapshots of the flow at different times and compares them to the results from [42]. Movie 2 in supplementary materials shows the full simulation of the dam break. In their work, a SPH-DEM formulation is used to simulate the same problem. The results are in good agreement, showing the potential of the PFEM-DEM method to capture such complex flows with the flexibility to keep a coarser mesh close to the grains. However, a fine mesh is still required to capture the free surface dynamics accurately. As the mesh nodes are advected, the volume of the fluid is not conserved. In this benchmark, the fluid volume is reduced up to 2.5% of its initial volume.

A quantitative study of this flow is feasible in the first step of the experiment, but becomes more delicate in the following ones as the flow takes a chaotic turn. To compare the results with the literature, the front positions of the fluid and grains are tracked. The front is defined as the position of the particle with the lowest y coordinate in the fluid or grain phase. To characterize the flow, the dimensionless Froude number is used, leading to dimensionless time and space coordinates based on the initial height of the column and the gravitational acceleration. Figure 12 shows the evolution of the front positions with respect to time. The accuracy of the PFEM-DEM method is demonstrated by the good agreement with the experimental results from [39].

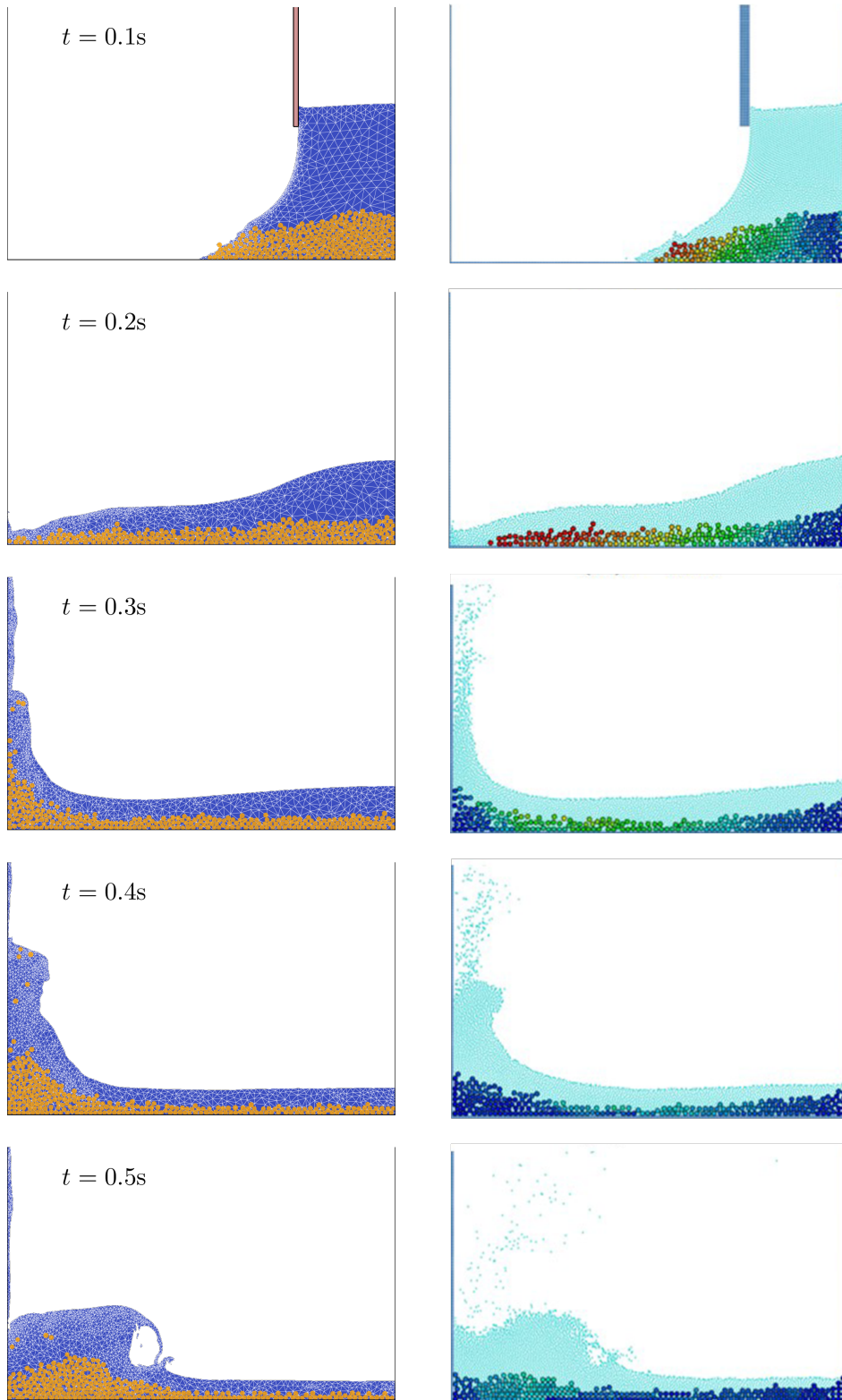


Figure 11: Time shots of the dam break simulation. On the left, results from the PFEM-DEM method are shown, and on the right, results from the SPH-DEM method are shown from Xie [42].

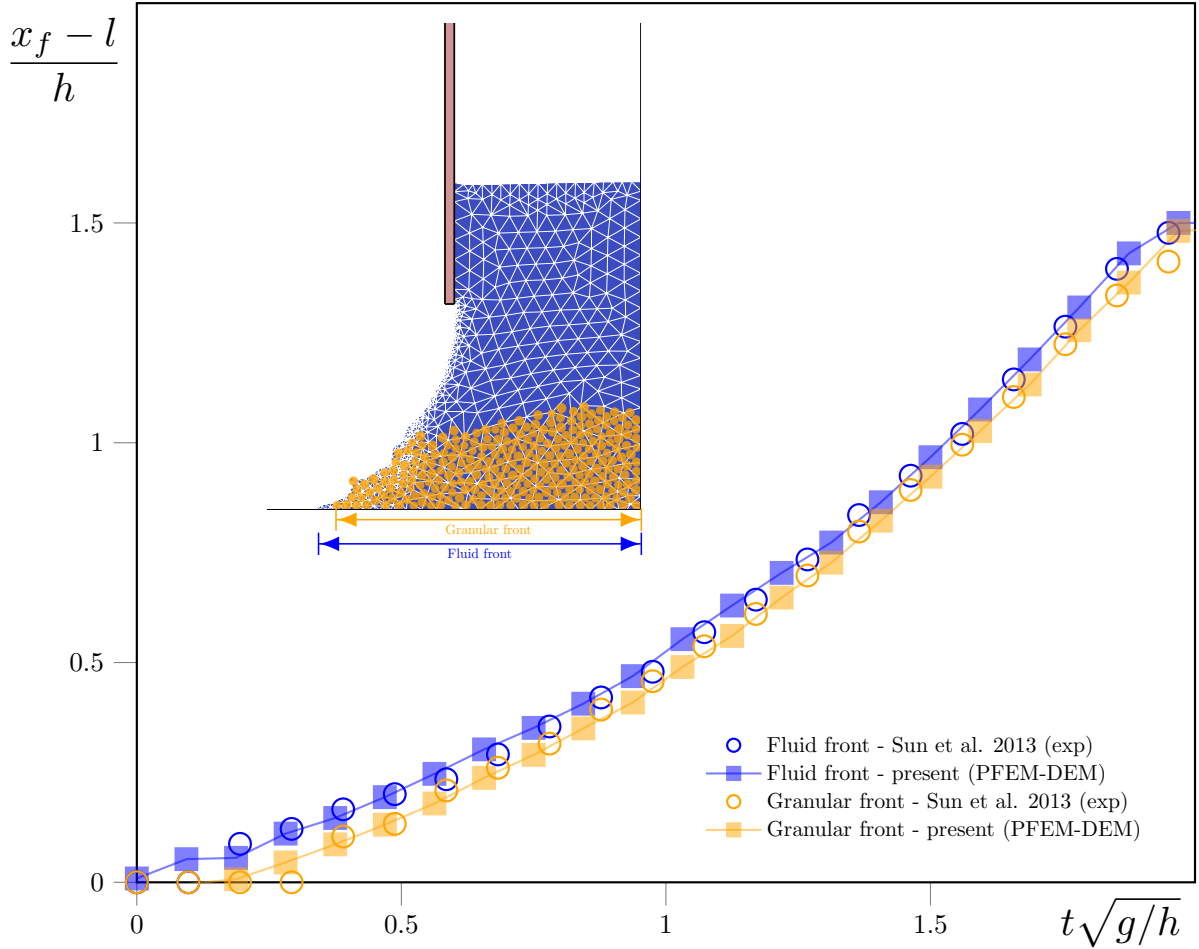


Figure 12: Time evolution of the granular front in orange and water front in blue for the dambreak. Numerical results, continuous lines, and squares, are compared to the experimental results, circles, from Sun [39].

Finally, a mesh sensitivity study is performed to demonstrate that the approach remains consistent when the fluid discretization becomes very refined relatively to the grain size. The same dam break simulations as described above are performed, with different minimum mesh sizes. Time steps are also adapted in order to respect a constant ratio of minimum mesh size over maximum velocity of the fluid. Figure 13 presents the evolution of the fluid front in time until it reaches the opposite wall. h_{\min} is defined as the minimum value of the mesh size, which is the size of the mesh along the free surface. This shows that the fluid mesh refinement level has little or no impact on the advective phenomena at the scale of the experiment. Figure 14 presents the variation in volume conservation for the fluid for the different levels of refinement. Here, it is clearly visible that the volume conservation improves as the mesh is refined and the time step decreases, showing that the problem is well-posed at the low time-step and small spatial discretization levels.

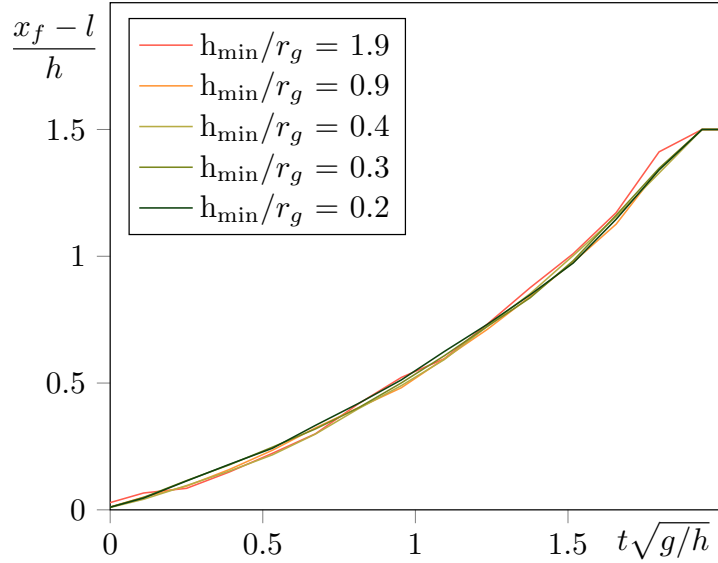


Figure 13: Time evolution of the water front for the dam break simulation for different ratios of the minimum mesh size h_{\min} (at the free surface) to the radius of the grains.

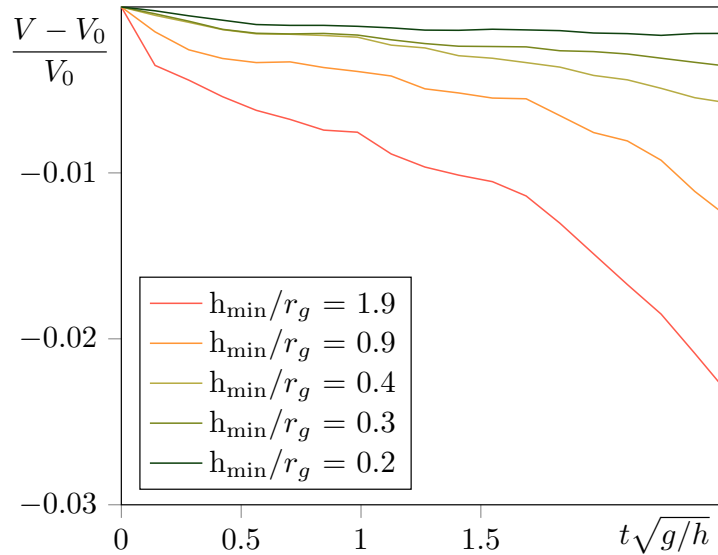


Figure 14: Time evolution of the total volume variation for the dam break simulation for different ratios of the minimum mesh size h_{\min} (at the free surface) to the radius of the grains.

5.2 Granular column collapse

In the second benchmark, a granular column, initially dry, collapses into a water bed. Similarly to the previous test case, a gate initially withholds the column, and at $t = 0$, is lifted upwards with a velocity of 1 m/s. The grains then fall into the water bed, causing a free surface impulse wave to travel in the direction opposite to the grain column.

A physical experiment was carried out in [35] to study the influence of different size parameters of both the grain column and water bed on the granular front as well as the resulting free surface wave. This allowed them to qualify the type of grain collapse, and to predict the resulting free surface wave on the water.

Three different experiments have been carried out, of which the main dimensional parameters are presented along with the initial setups in Figure 15. For the granular phase, spherical grains with an average diameter of 5 mm are used, with a polydispersity coefficient of 1.2. The density of the grains is

2500 kg/m³, and a Coulomb friction law with a coefficient equal to 0.9 defines the friction between all rigid bodies. For the water phase, free-slip boundary conditions are considered along the solid walls, and the surface tension coefficient along the free surface is set to 0.0072N/m.

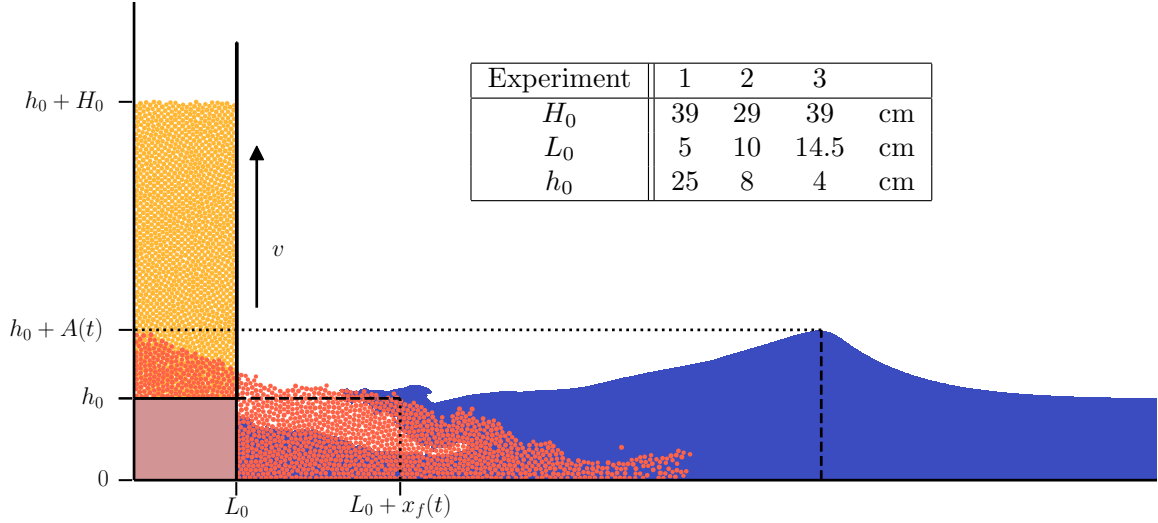


Figure 15: Granular column collapse test case setup.

An initial Froude number, as defined above, can be used to qualify the flow. However, as suggested in [34], a better choice of characteristic velocity than the equivalent free-fall velocity, is the maximum horizontal velocity v_{fm} of the granular front.

$$\text{Fr}_f = \frac{v_{fm}}{\sqrt{gh_0}}.$$

The reason for this different choice of velocity to describe the flow comes from the fact that the main driving force of the free surface wave is the horizontal push of the grains, and not their vertical drop as the column collapses. Though this velocity depends on the initial height of the column, it also depends on its initial width L_0 . The work of [35] has allowed them to distinguish three different regimes as follows, based on the Froude number (Fr_f) defined with the maximum horizontal velocity of the front:

- $\text{Fr}_f \lesssim 0.35$: Nonlinear transition wave
- $0.35 \lesssim \text{Fr}_f \lesssim 0.87$: Solitary non-breaking wave
- $0.87 \lesssim \text{Fr}_f$: Transient bore wave

To validate the proposed method, three different experiments have been carried out, each corresponding to one of the three regimes. The amplitude of the wave and the granular front position are tracked to validate the wave regime and the grains dynamics. The results are compared to the experimental results from [35]. The setup of each experiment, as well as the corresponding Froude numbers, are summarized in the table of Figure 15.

In the first case, the first regime is indeed observed as the free surface is dominated by a nonlinear transition wave, as seen in Figure 16. The full simulation video can be found in Movie 3 of supplementary materials. In this case, grains become fully submerged in the fluid and the granular front goes to zero. In the second case, the solitary non-breaking wave is observed generated by the granular motion, as seen in Figure 17, with Movie 4 of the supplementary materials showing the full simulation. The fall of

grains is not sufficient to submerge all the grains and the granular front is still visible once the wave has passed. The wave takes time to roll over itself, and the wave amplitude remains close to a constant value until then. In the last case, a bore wave is observed as seen in Figure 18 and Movie 5 of supplementary materials. The grains motion expelled a significant amount of fluid, leading to a nonlinear wave regime which quickly rolls over itself and breaks. A part of the fallen grains remains dry as the water has been expelled and two internal friction angles can be observed in the grains, one for the dry grains, and one for the submerged grains.

Qualitatively, the three regimes are accurately captured by the numerical simulations. However, disparities are observed in the granular front position, but this can be attributed to the uncertainty in the measure of the granular front position. Indeed, to measure the granular front, the furthest grain at a height of $y = h_0$ is taken, as illustrated in Figure 15. With the aim of computing the maximum horizontal velocity of the grains at the free surface, responsible of generating the impulse wave, this measure is the most relevant option. However, this choice does not lead to consistent results if grains are fully submerged in the fluid, as the granular front is not visible anymore. If one is only interested in computing the maximum position reached by the grains inside the flow, an alternative, more robust measure would be to take the runout distance of the avalanche, defined as the position of the farthest grain still connected to the contact network [9]. The order of magnitude of the wave amplitude is well captured, but the amplitude is slightly overestimated. This can be attributed to a higher grains velocity in the numerical simulations, as the grains are not subject to the same friction as in the physical experiments. Although the three regimes are correctly captured qualitatively and respect the bounds, we note some discrepancies with the obtained Froude numbers. The bi-dimensional nature of the simulations is one of the reasons for these differences. Indeed, the experiments are performed in a three-dimensional setup with monodisperse spherical grains. The numerical representation assume discs with a polydispersity coefficient of 1.2. The drag constitutive law is chosen to mimic the one from sphere with a cross section associated to cylinder. The polydispersity ratio is a compromise between the need to have a good representation of the granular deposit and to avoid crystallization effects. Additionally, the friction between grains and between grain and wall could be calibrated to better mimic the experiments. Finally, the high variance of the granular fronts due to the divided nature of the solid phase could also lead to discrepancies in the numerical results. From the numerical setups used in this paper, the obtained values for Fr_f are presented in table 1. Although the results are not exactly matching those of the experiments, the regimes are still detected correctly within the bounds proposed by [35].

Experiment	Fr_f (PFEM-DEM)	Fr_f (exp., Sarlin et al.)
1	0.27	0.19
2	0.83	0.65
3	1.93	1.39

Table 1: Froude numbers based on the maximum horizontal velocity of the grain column for the different cases, compared with the experimental data.

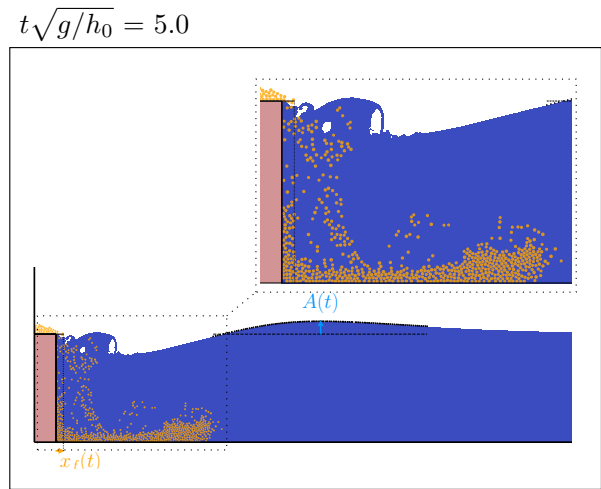
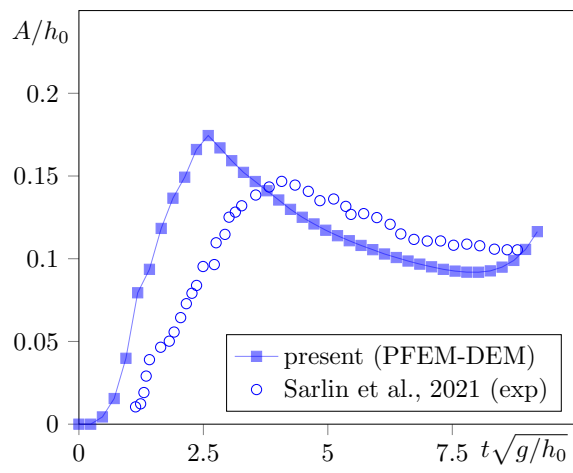
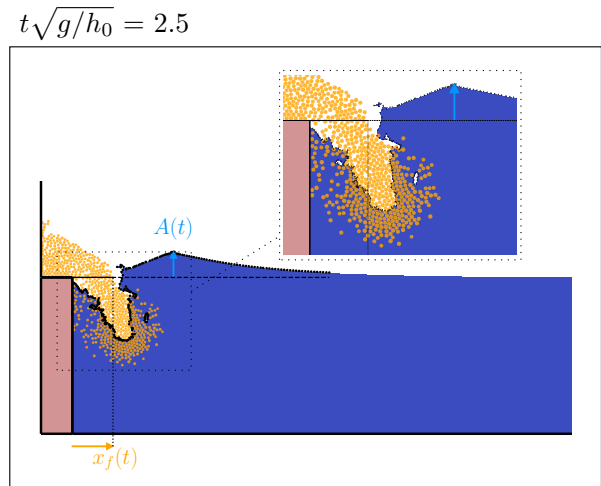
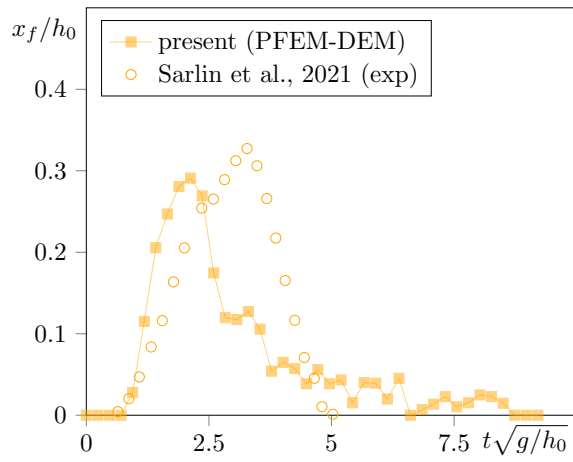


Figure 16: Granular collapse: case 1

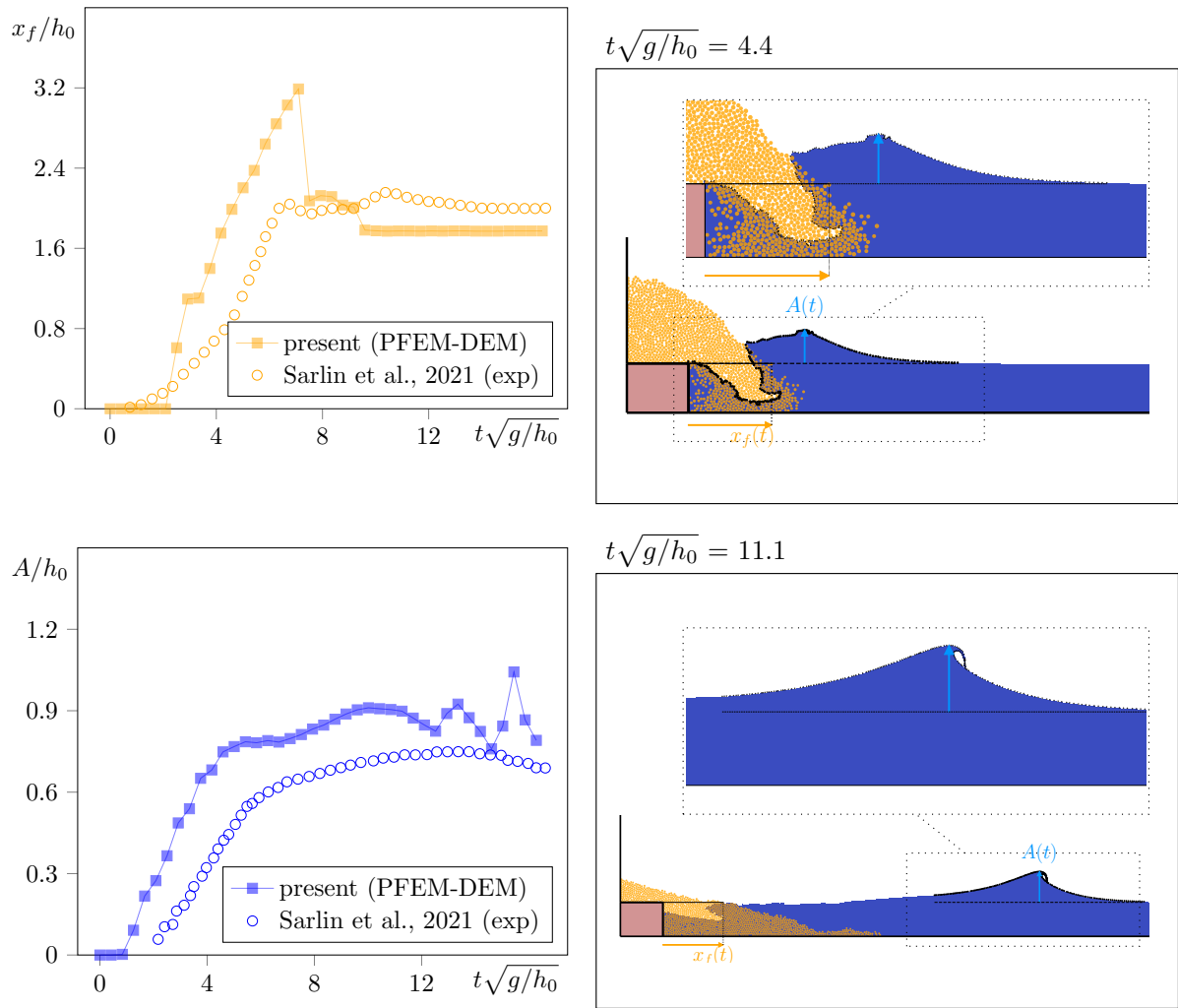


Figure 17: Granular collapse: case 2

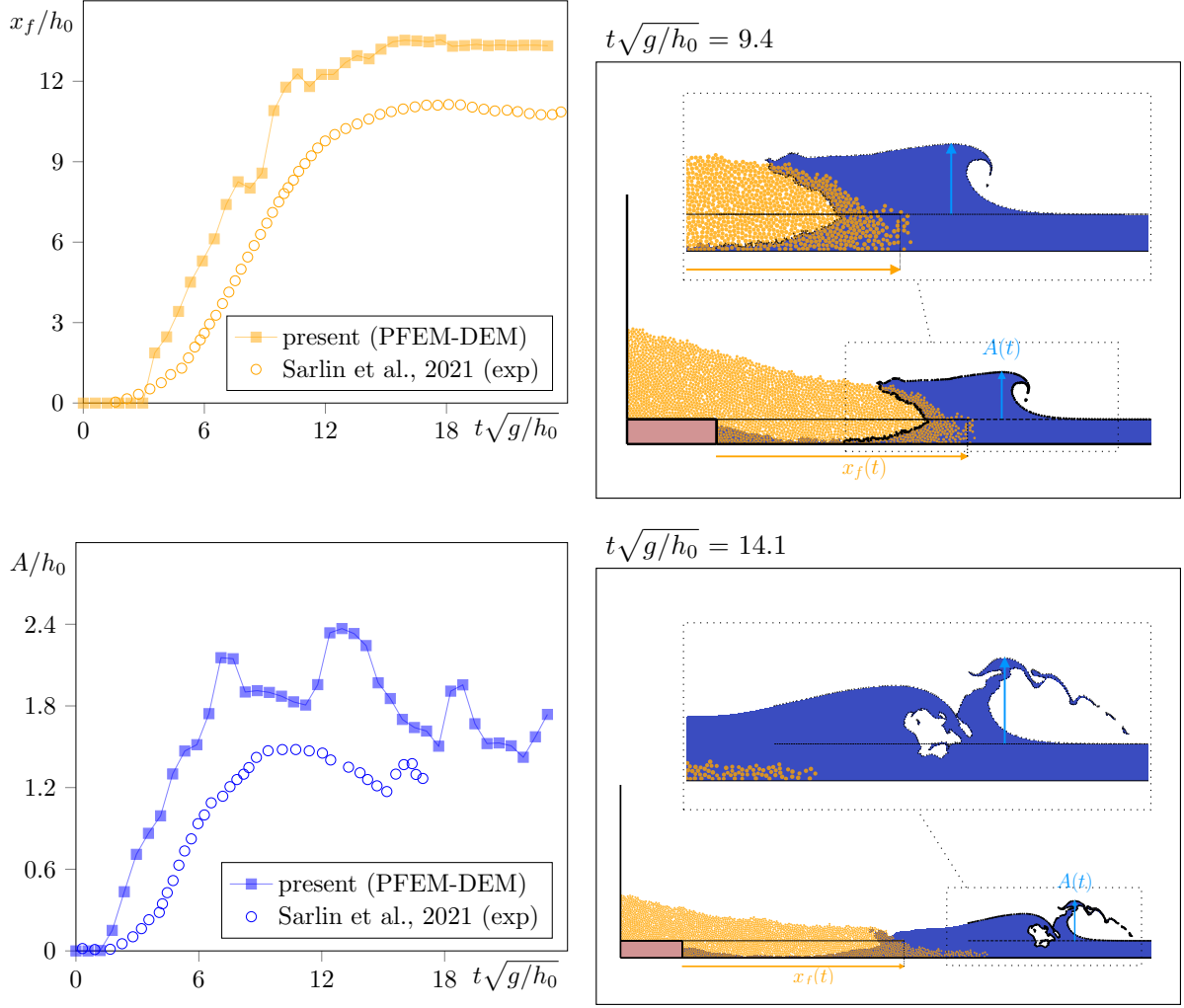


Figure 18: Granular collapse: case 3

6 Lituya bay landslide and tsunami

To investigate the robustness and accuracy of the proposed model, a realistic case, the Lituya Bay landslide and tsunami, is studied. On 10 July 1958, an earthquake along the Fairweather fault caused a large landslide above Lituya Bay in Alaska. The loose rock slid downhill and hit the waters of Lituya Bay, creating a 60m wave that reached heights of over 500m on the opposite shore. The tsunami resulted in human casualties and homes were destroyed. As mountains become increasingly unstable due to climate change, such events are expected to become more frequent. Understanding and predicting the impact of such events is crucial to mitigate the risks. The presented numerical method is a suitable tool for such phenomena, as both the landslide and the tsunami can be simulated and analyzed, providing a fine description of both the grain dynamics and the wave motion. To quantitatively compare the results with the real event, the numerical results are compared with the experimental results of [17]. In their study, a 1:675 scale experiment of the Lituya Bay landslide and tsunami was carried out in order to better quantify the event.

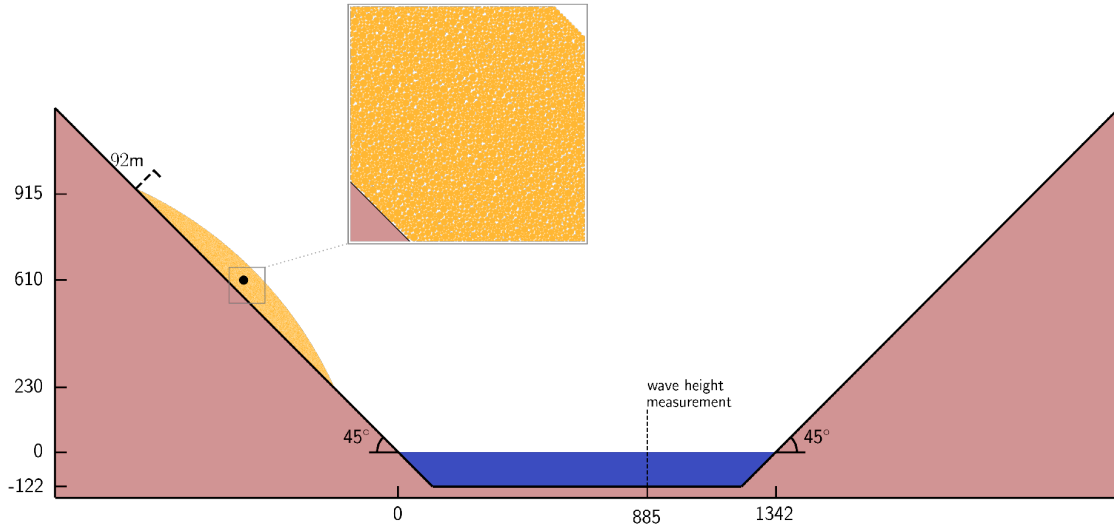


Figure 19: Lituya bay landslide and tsunami setup.

The setup of the experiment is shown in Figure 19. According to the estimated amount of rock that was torn from the hill, a mass of grains 970m long and 92m thick, is positioned 230m above the water level. This gives a total mass per unit thickness of 98.5×10^3 t/m. The grains have a density of 2.64 t/m³, and a polydispersity ratio of 3 allows the bulk to be more compact. The average grains radius is set to 1.35m, in order to match the 2 mm radius used in [17], put to real-life scale. This results in a total of 27960 grains. The friction coefficient between the grains and with the walls is set to $\mu = 0.93$, which corresponds to an effective internal friction angle of 43°. The water bed, representing a cross section of the Gilbert Inlet in the Lituya Bay, has a depth of 122 m, and a total length of 1342 m. Both shores rise with an angle of 45°. At $t = 0$, the grain mass is set in motion. The Froude number is here also the relevant dimensionless number to relate the impact of the grains to the potential energy stored in the water bed. Considering the mean velocity v_g of the grains as they impact the water, estimated at 110m/s in [17], and the water depth of the bay, equal to 122m, the resulting Froude number is equal to

$$\text{Fr} = \frac{v_g}{\sqrt{gh}} = 3.18.$$

In this case, the wave is expected to break, as the Froude number is largely superior to the limit proposed in the previous testcase for the transition from non-breaking to breaking waves. The initial height of the centroid of the landslide has been set to 610m in order to match the mean impact velocity v_g of the physical experiment.

Some snapshots of the simulation are presented in Figure 20. Movie 6 in the supplementary materials shows the full simulation. The wave hits the opposite shore before breaking, as has also been observed in [17]. The height reached on the opposite shore is tracked in Figure 21. Observations at Lituya Bay stated the inertia of the wave was sufficient to damage trees at over 500m. The numerical model indeed shows that such a height is reached by the wave. The maximal point reached a height of around 750m. This value may be overestimated as water is assumed to slide freely along the boundary. When the wave returns in the opposite direction, a sloshing phenomenon appears, and the wave reflects multiple times against the opposing shores. To track if the model is able to capture these reflectives waves, the wave amplitude at a position of 885m from the initial shore is compared to the experimental data from [17] at Figure 22. The dimensionless height and time are computed using the initial water depth h_0 as the reference height and g the gravitational acceleration. The Lagrangian formulation is able to accurately capture the main trends in the wave dynamics. However, as the domain is advected and meshed at each iteration, the water volume is not conserved. The initial impact of the grain on the water bed leads to high deformations and the formation of a first wave. These deformations are the main source of volume

loss. The maximal volume variation is around 10% of the initial volume.

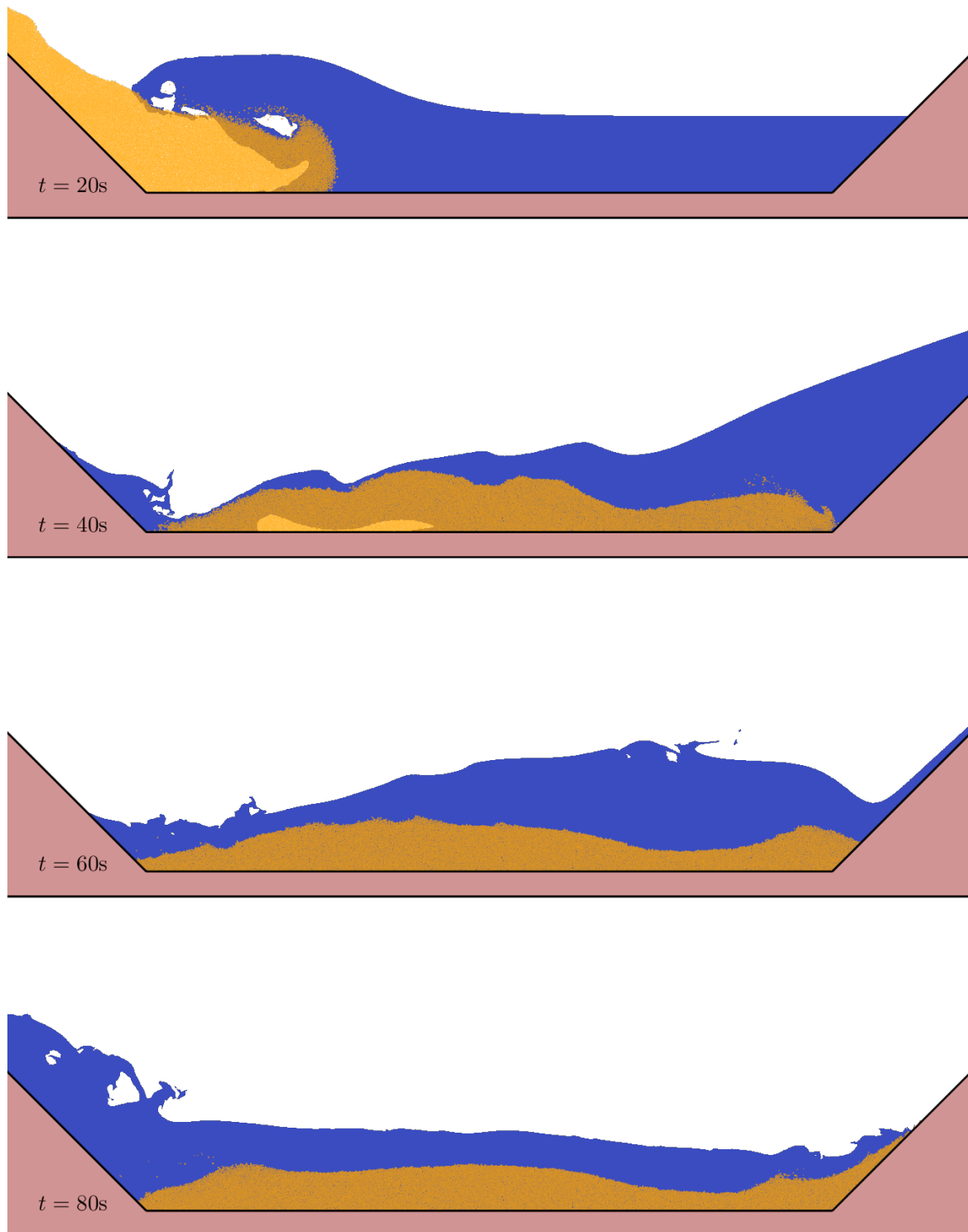


Figure 20: Snapshots of the Lituya bay landslide and the wave generated by the fallen rocks at time 20, 40, 60 and 80s.

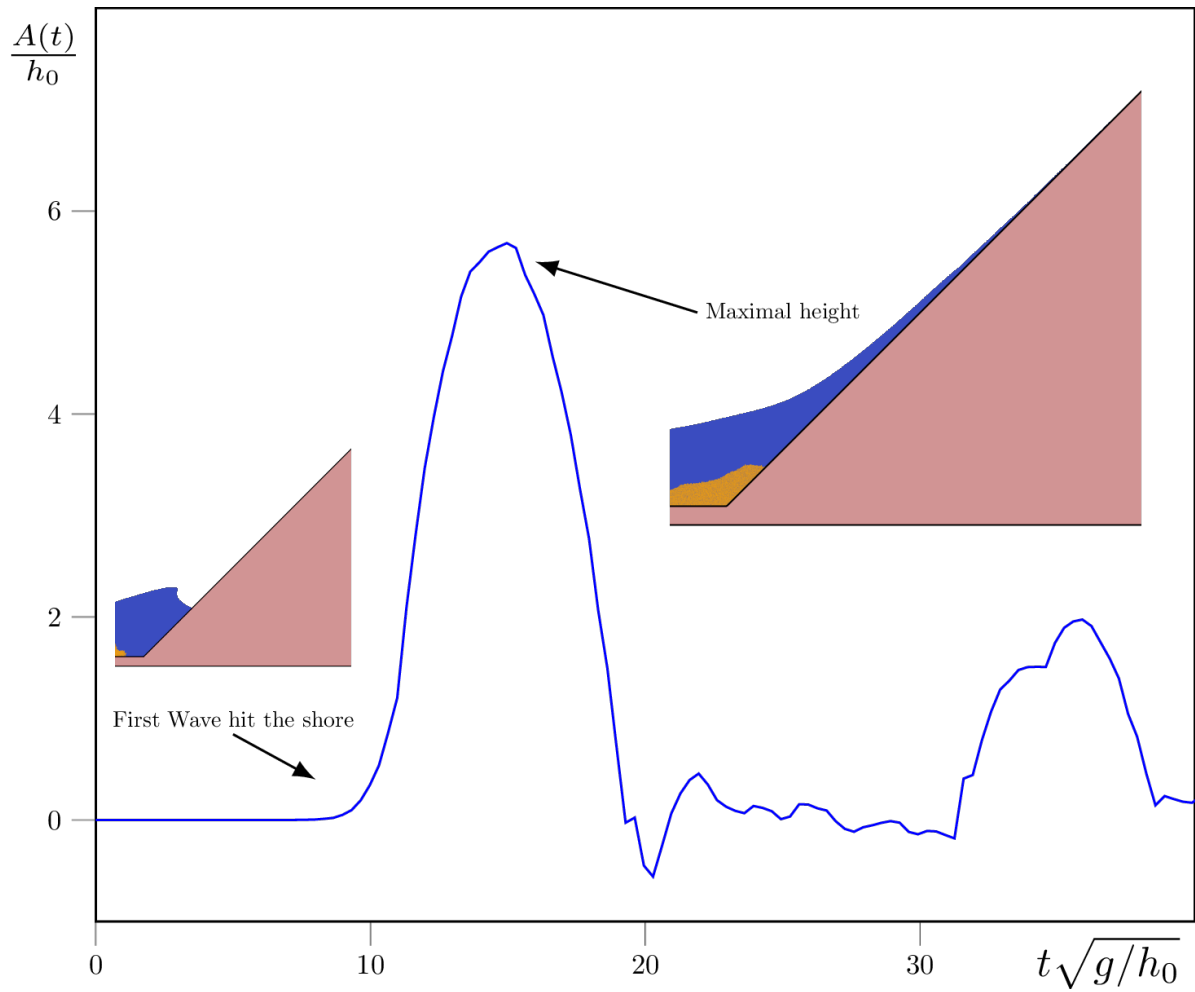


Figure 21: Evolution of the wave amplitude on the opposite shore. Dimensionless height is defined by the initial depth h_0 and the gravitational accelerating is used to define a dimensionless time.

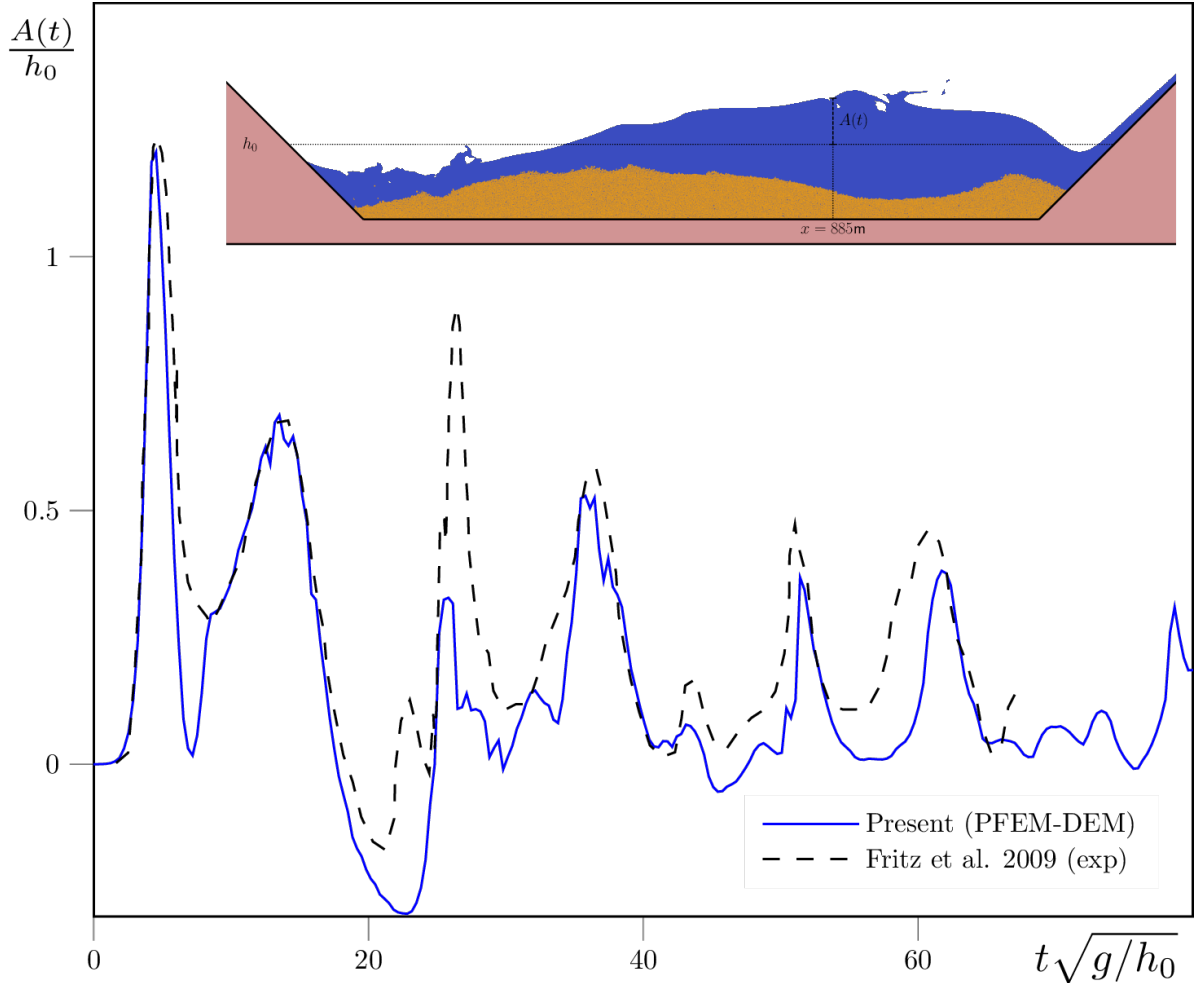


Figure 22: Wave height evolution at $x = 885\text{m}$. Numerical results, the continuous blue line, is compared to the experimental results from [17], dotted black curve. The dimensionless height and time are computed using the initial bathymetry h_0 as the reference height and g the gravitational acceleration.

7 Conclusions

This paper presents a coupled Lagrangian model to simulate immersed granular flows with free surfaces and moving domains. The method is based on a coupling between a particle finite element method (PFEM) solver and a discrete element method (DEM) solver. The coupling provides robustness and flexibility to the simulation. As the PFEM solver is based on a Lagrangian formulation, it can handle strongly deforming domains and free surfaces. The DEM solver, on the other hand, is well suited for granular problems and provides insight into the contact dynamics. The Volume-Averaged formulation avoids the need to provide constitutive laws for the granular phase as it is directly captured by the contact dynamics. However, a constitutive law is required to model the fluid-grain interaction. In addition, the mesh size can be chosen independently for each phase, allowing the mesh to be refined only where it is needed. In practice, a fine mesh is used close to the free surface to capture large deformations and topological changes, while a coarser mesh is used in the bulk of the domain.

The accuracy of the method is assessed on a few benchmarks. First a dam break consisting of grains and water is simulated to serve as a verification of the numerical model. The results show good agreement with experimental data and existing numerical methods to track the free surface and the granular front. Next, to investigate the behaviour of the method in the presence of strong deformations, a granular column collapse is simulated. Depending on the geometry of the granular column and the depth of the water bed, leading to different fall velocities of the grains, the wave dynamics can be very different.

Experimental results from the literature [35] proposed a characterization based on the flow’s Froude number, and divided the experiments into three regimes. These three regimes are well captured by the proposed method, validating the method and showing the capability of the approach to solve complex phenomena such as high amplitude free surface waves triggered by landslides.

Finally, the method is applied to a realistic event, the 1958 Lituya Bay landslide and tsunami. The results show that the method can capture the main features of the event, such as the landslide and the subsequent tsunami. Moreover, the complex behaviour is still well captured when the wave begins to reflect on the opposite shore.

The results presented in this work show that the method can be applied to a wide range of problems, but there are still some limitations and room for improvement. For one thing, the fluid’s volume is not conserved. This error is mainly due to the fact that the node advection scheme used in the method is not conservative. Additionally, remeshing at each time step introduces some numerical diffusivity, and the fact of defining the domain based on the α -shape of the point cloud can cause unphysical deformations. This can lead to some inaccuracies in the results, especially if the free surface is not fully resolved. To mitigate this, the mesh size is refined close to the free surface. At present, the method is limited to two dimensions, but an extension to three dimensions is planned and no major differences are expected. The multi-scale approach can also have some limitations as its computational cost scales with both the number of grains and the number of fluid particles. This can become a bottleneck for real scale applications as the number of particles can become very large. In this case, a parallel implementation of the method is required, or the use of a continuous representation of the grains.

Although the applications are limited to landslide-related phenomena in this paper, the approach can be exploited on a wide variety of physical experiments. For example, it could be applied to mixing problems in tanks, soil digging problems, or even small-scale applications such as injector-induced bubble flows.

8 Acknowledgments

The authors acknowledge that Michel Henry and Thomas Leysens contributed equally both to the research and writing of this paper. Thomas Leysens is a Research Fellow of the F.R.S.-FNRS. Computational resources have been provided by the supercomputing facilities of the Université catholique de Louvain (CISM/UCL) and the Consortium des Équipements de Calcul Intensif en Fédération Wallonie Bruxelles (CÉCI) funded by the Fond de la Recherche Scientifique de Belgique (F.R.S.-FNRS) under convention 2.5020.11 and by the Walloon Region. This project has received funding from the European Research Council (ERC) under the European Union’s Horizon research and innovation program (Grant agreement No. 101 071 255).

References

- [1] Stéphane Abadie et al. “Numerical simulation of waves generated by landslides using a multiple-fluid Navier–Stokes model”. In: *Coastal engineering* 57.9 (2010), pp. 779–794.
- [2] T. B. Anderson and Roy Jackson. “Fluid Mechanical Description of Fluidized Beds. Equations of Motion”. In: *Industrial & Engineering Chemistry Fundamentals* 6.4 (Nov. 1967), pp. 527–539. ISSN: 0196-4313. DOI: 10.1021/i160024a007.
- [3] Aaron S. Baumgarten and Ken Kamrin. “A General Fluid–Sediment Mixture Model and Constitutive Theory Validated in Many Flow Regimes”. In: *Journal of Fluid Mechanics* 861 (Feb. 2019), pp. 721–764. ISSN: 0022-1120, 1469-7645. DOI: 10.1017/jfm.2018.914. (Visited on 08/30/2022).
- [4] Marco Lucio Cerquaglia et al. “Free-slip boundary conditions for simulating free surface incompressible flows through the particle finite element method”. In: *International Journal for numerical methods in engineering* 110.10 (2017), pp. 921–946.

- [5] Chuan Miao Chen and Vidar Thomée. “The lumped mass finite element method for a parabolic problem”. In: *The ANZIAM Journal* 26.3 (1985), pp. 329–354.
- [6] L Paul Chew. “Guaranteed-quality mesh generation for curved surfaces”. In: *Proceedings of the ninth annual symposium on Computational geometry* (1993), pp. 274–280.
- [7] Daniel A. Clarke et al. “Investigation of Void Fraction Schemes for Use with CFD-DEM Simulations of Fluidized Beds”. In: *Industrial & Engineering Chemistry Research* 57.8 (Feb. 2018), pp. 3002–3013. ISSN: 0888-5885. DOI: 10.1021/acs.iecr.7b04638. (Visited on 08/26/2024).
- [8] Matthieu Constant et al. “Implementation of an Unresolved Stabilised FEM-DEM Model to Solve Immersed Granular Flows”. In: *Computational Particle Mechanics* (Sept. 2018). ISSN: 2196-4378, 2196-4386. DOI: 10.1007/s40571-018-0209-4. (Visited on 03/01/2019).
- [9] Nathan Coppin et al. “Collapse dynamics of two-dimensional dry and immersed granular columns of elongated grains”. In: *Physical Review Fluids* 8.9 (2023), p. 094303.
- [10] Nathan Coppin et al. “Numerical analysis of the drag on a rigid body in an immersed granular flow”. In: *Computational Particle Mechanics* 9.3 (2022), pp. 393–406.
- [11] Frédéric Dubois, Vincent Acary, and Michel Jean. “The Contact Dynamics Method: A Nonsmooth Story”. In: *Comptes Rendus Mécanique. The Legacy of Jean-Jacques Moreau in Mechanics / L’héritage de Jean-Jacques Moreau En Mécanique* 346.3 (Mar. 2018), pp. 247–262. ISSN: 1631-0721. DOI: 10.1016/j.crme.2017.12.009. (Visited on 10/07/2021).
- [12] Herbert Edelsbrunner, David Kirkpatrick, and Raimund Seidel. “On the shape of a set of points in the plane”. In: *IEEE Transactions on information theory* 29.4 (1983), pp. 551–559.
- [13] Toni El Geitani and Bruno Blais. “Quadrature-centered averaging scheme for accurate and continuous void fraction calculation in computational fluid dynamics-discrete element method simulations”. In: *Industrial & Engineering Chemistry Research* 62.12 (2023), pp. 5394–5407.
- [14] Alessandro Franci and Massimiliano Cremonesi. “On the effect of standard PFEM remeshing on volume conservation in free surface fluid flow problems”. In: *Computational particle mechanics* 4.3 (2017), pp. 331–343.
- [15] Alessandro Franci et al. “3D simulation of Vajont disaster. Part 1: Numerical formulation and validation”. In: *Engineering Geology* 279 (2020), p. 105854.
- [16] Alessandro Franci et al. “PFEM-DEM for particle-laden flows with free surface”. In: *Computational Particle Mechanics* 7 (2020), pp. 101–120.
- [17] Hermann M Fritz, Fahad Mohammed, and Jeseon Yoo. “Lituya Bay landslide impact generated mega-tsunami 50 th Anniversary”. In: *Tsunami Science four years after the 2004 Indian ocean tsunami: Part II: Observation and data analysis* (2009), pp. 153–175.
- [18] Toni El Geitani, Shahab Golshan, and Bruno Blais. “A High-Order Stabilized Solver for the Volume Averaged Navier-Stokes Equations”. In: *International Journal for Numerical Methods in Fluids* 95.6 (2023), pp. 1011–1033. ISSN: 1097-0363. DOI: 10.1002/fld.5182. (Visited on 10/01/2024).
- [19] Michel Henry et al. “Multiscale FEM-DEM model for spontaneous droplet digging in a hot granular bed”. In: *International Journal of Heat and Mass Transfer* 241 (2025), p. 126755.
- [20] Cyril W Hirt and Billy D Nichols. “Volume of fluid (VOF) method for the dynamics of free boundaries”. In: *Journal of computational physics* 39.1 (1981), pp. 201–225.
- [21] Thomas JR Hughes, Leopoldo P Franca, and Marc Balestra. “A new finite element formulation for computational fluid dynamics: V. Circumventing the Babuška-Brezzi condition: A stable Petrov-Galerkin formulation of the Stokes problem accommodating equal-order interpolations”. In: *Computer methods in applied mechanics and engineering* 59.1 (1986), pp. 85–99.
- [22] Thomas JR Hughes, Wing Kam Liu, and Thomas K Zimmermann. “Lagrangian-Eulerian finite element formulation for incompressible viscous flows”. In: *Computer methods in applied mechanics and engineering* 29.3 (1981), pp. 329–349.

- [23] Michel Jean, Vincent Acary, and Yann Monerie. “Non-Smooth Contact Dynamics Approach of Cohesive Materials”. In: *Philosophical Transactions of The Royal Society A: Mathematical, Physical and Engineering Sciences* 359 (Dec. 2001), pp. 2497–2518. DOI: 10.1098/rsta.2001.0906.
- [24] H. Kruggel-Emden et al. “Review and Extension of Normal Force Models for the Discrete Element Method”. In: *Powder Technology* 171.3 (Feb. 2007), pp. 157–173. ISSN: 0032-5910. DOI: 10.1016/j.powtec.2006.10.004. (Visited on 02/21/2022).
- [25] Thomas Leysens et al. “A Delaunay refinement algorithm for the particle finite element method applied to free surface flows”. In: *International Journal for Numerical Methods in Engineering* (2024), e7554.
- [26] Abhilash Reddy Malipeddi, C Alberto Figueroa, and Jesse Capecelatro. “Volume filtered FEM-DEM framework for simulating particle-laden flows in complex geometries”. In: *arXiv preprint arXiv:2311.15989* (2023).
- [27] Jia Mao et al. “A resolved CFD–DEM approach for the simulation of landslides and impulse waves”. In: *Computer Methods in Applied Mechanics and Engineering* 359 (2020), p. 112750.
- [28] Célestin Marot, Jeanne Pellerin, and Jean-François Remacle. “One machine, one minute, three billion tetrahedra”. In: *International Journal for Numerical Methods in Engineering* 117.9 (2019), pp. 967–990.
- [29] Donald Meagher. “Efficient synthetic image generation of arbitrary 3-D objects”. In: *Proceeding of the IEEE Conference on Pattern Recognition and Image Processing*. Vol. 473. 1982.
- [30] Joe J Monaghan. “Smoothed particle hydrodynamics”. In: *Reports on progress in physics* 68.8 (2005), p. 1703.
- [31] Eugenio Onate et al. “Advances in the particle finite element method (PFEM) for solving coupled problems in engineering”. In: *Particle-based methods: fundamentals and applications* (2011), pp. 1–49.
- [32] Eugenio Oñate et al. “The particle finite element method—an overview”. In: *International Journal of Computational Methods* 1.02 (2004), pp. 267–307.
- [33] Andrea Pasqua, Alessandro Leonardi, and Marina Pirulli. “Coupling Depth-Averaged and 3D numerical models for the simulation of granular flows”. In: *Computers and Geotechnics* 149 (2022), p. 104879.
- [34] Manon Robbe-Saule et al. “Experimental investigation of tsunami waves generated by granular collapse into water”. In: *Journal of Fluid Mechanics* 907 (2021), A11.
- [35] Wladimir Sarlin et al. “Nonlinear regimes of tsunami waves generated by a granular collapse”. In: *Journal of Fluid Mechanics* 919 (2021), R6.
- [36] Severin Strobl, Arno Formella, and Thorsten Pöschel. “Exact Calculation of the Overlap Volume of Spheres and Mesh Elements”. In: *Journal of Computational Physics* 311 (Apr. 2016), pp. 158–172. ISSN: 0021-9991. DOI: 10.1016/j.jcp.2016.02.003. (Visited on 11/20/2023).
- [37] Pratik Suchde and Jörg Kuhnert. “Point cloud movement for fully Lagrangian meshfree methods”. In: *Journal of Computational and Applied Mathematics* 340 (2018), pp. 89–100.
- [38] Deborah Sulsky, Zhen Chen, and Howard L Schreyer. “A particle method for history-dependent materials”. In: *Computer methods in applied mechanics and engineering* 118.1-2 (1994), pp. 179–196.
- [39] Xiaosong Sun, Mikio Sakai, and Yoshinori Yamada. “Three-dimensional simulation of a solid–liquid flow by the DEM–SPH method”. In: *Journal of Computational Physics* 248 (2013), pp. 147–176.
- [40] Mark Sussman et al. “An improved level set method for incompressible two-phase flows”. In: *Computers & Fluids* 27.5-6 (1998), pp. 663–680.
- [41] Steven N Ward. “Landslide tsunami”. In: *Journal of Geophysical Research: Solid Earth* 106.B6 (2001), pp. 11201–11215.

- [42] Fengze Xie, Weiwen Zhao, and Decheng Wan. “Numerical simulations of liquid-solid flows with free surface by coupling IMPS and DEM”. In: *Applied Ocean Research* 114 (2021), p. 102771.